The Open Cassegrain Antenna: Part I. Electromagnetic Design and Analysis

By J. S. COOK, E. M. ELAM and H. ZUCKER

(Manuscript received May 14, 1965)

The open cassegrain antenna combines an asymmetric cassegrain reflector system with antenna rotation about two non-orthogonal axes. The compact configuration provides well-controlled radiation with full hemispheric coverage.

A comprehensive analysis of the antenna geometrical and radiation characteristics has been made, and an experimental antenna with 40-inch aperture, operating at 60 gcs, has been constructed and measured electrically. Agreement was obtained between the computed and measured characteristics of the antenna and its components. By computation, it is found that the aperture efficiency of the experimental antenna is 70.4 per cent, the antenna efficiency (neglecting ohmic loss) is 65 per cent, and based on measured subreflector radiation patterns, the noise temperature due to spillover at the main reflector is less than 4°K.

I. INTRODUCTION

The open cassegrain antenna configuration is shown in Fig. 1. Its optical geometry is straight forward, consisting of hyperboloid and paraboloid surfaces, but it has the distinguishing characteristic that the axes of rotational symmetry of the sub- and main-reflector surfaces do not coincide. Fig. 2 shows a view of the antenna looking down the beam axis. The projected aperture is circular and no aperture blocking is introduced by the subreflector or its support structure (not shown in Fig. 2), hence the name open cassegrain.

Non-orthogonal beam steering axes are used. The antenna is directed at zenith in Fig. 1(a) and at its minimum elevation of −5° in Fig. 1(b). The lowest elevation excursion is determined by the angle of the slant axis which is coincident with the "secondary optical" axis and is in-

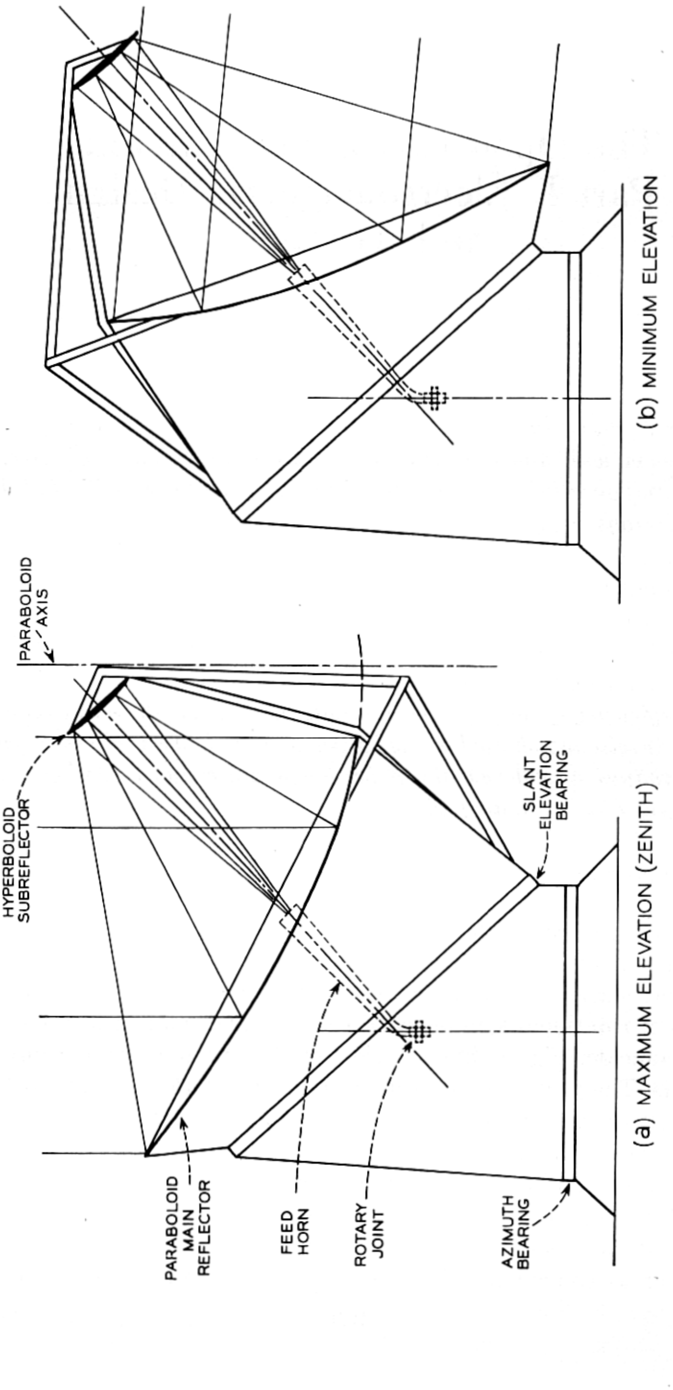

(a) MAXIMUM ELEVATION (ZENITH)

(b) MINIMUM ELEVATION

Fig. 1 — Open cassegrain antenna.

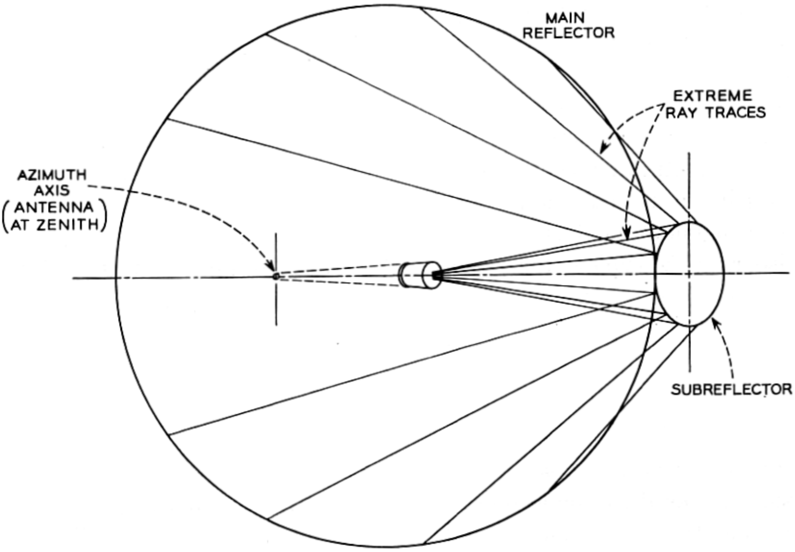

Fig. 2 — Antenna view from the direction of main beam.

clined 42.5° from the horizontal. The conical feed horn is attached to the azimuth unit and remains fixed when the antenna rotates about its slant axis. This unusual configuration is motivated by the desire to bring the antenna feed to a convenient equipment location as directly as possible, and to keep the structure small and easily enclosed so the antenna can be operated reliably without the protection of a radome.

Both electrical and structural characteristics of the open cassegrain have been studied. The particular antenna design that was used as a model for the studies was derived by balancing electrical against structural considerations to arrive (somewhat arbitrarily) at a configuration that would meet the general requirements of a wide band 4-gcs satellite communications link. A close interdependence exists between these two aspects of antenna design presented in this issue as Part I and Part II of the open cassegrain antenna study.

The following section of Part I considers the antenna system and the background against which antenna characteristics must be chosen. Section III presents the geometrical interrelationships of the reflector surfaces which set the ground rules for electrical and structural tradeoffs. The coordinates and geometrical expressions necessary for the electromagnetic analysis that follows are also presented in Section III. The analysis of the radiation characteristics is presented in Section IV, followed in Section V by corresponding measurements of a 60-gc antenna. The concluding section contains a brief summary of antenna performance.

Dual-mode excitation of the circular-cone feed horn (TE_{11} and TM_{11} modes),[1] while not necessary for operation of the open cassegrain, brings about enough improvement in its characteristics over simple TE_{11} mode excitation that combined excitation has been assumed throughout the electromagnetic analysis. An improvement of roughly 1 db in signal-to-noise ratio is typical for a sensitive (maser) receiving system. Mode conversion techniques are investigated in a separate paper.[2]

II. ANTENNA SYSTEM CONSIDERATIONS

2.1 *Antenna Noise*

The essential low-noise advantage of the open cassegrain comes as a result of operating the antenna without a radome; but the *rf* configuration and the slant mount combine to make the antenna itself an inherently low-noise device.

The excess noise received by the more common symmetrical cassegrain (where the subreflector is centered on the paraboloid axis) comes mostly from three sources: (1.) scattering from the subreflector support (and subreflector blocking if it's excessively large), (2.) radiation past the edge of the subreflector, and (3.) radiation past the edge of the main reflector. The amount of extraneous radiation from these sources can be selectively minimized by using near-field subreflector illumination,[3] special subreflector supports, reflector skirts, etc., but it is difficult to avoid receiving a certain amount of extra thermal noise, particularly as the antenna swings down toward the horizon.

Since the open cassegrain subreflector is located outside the main beam, the extraneous scattering is minimized. Subreflector spillover is confined to an elevation of about 30° to 55° above the horizon regardless of the antenna position.

This leaves only the main reflector spillover as a major source of excess antenna noise, and it is essentially independent of elevation angle.

2.2 *Signal-to-Noise Optimization*

The quality of a low-noise antenna must be evaluated in terms of the system it serves. The receiver system quality is measured by its signal-to-noise ratio, which is proportional to the antenna gain and inversely proportional to the total system noise.

In clear weather, sky noise varies from 3°K at zenith to about 20°K at 7.5° elevation angle.[4] A maser receiver and its plumbing is likely to add 6 or 8°K to that. Thus, for a high-quality receiving system, the contribution to system noise exclusive of extraneous pickup from the antenna is about 10°K at zenith and increases to 27°K at the nominally minimum useful elevation. It is against this background that one must choose the antenna characteristics. One would not be willing to pay a great deal, for example, to improve the excess antenna noise from 5°K to 3°K since that would improve the signal-to-noise ratio only 0.6 db at zenith where it is needed least, and 0.3 db or less at the extremes of the satellite pass. On the other hand, one would like to have even that much improvement if it is easily achieved.

The open cassegrain lends itself to the optimization of the trade-off between aperture efficiency and excess noise. For a given projected aperture, the parameters to be optimized are: (1.) paraboloid focal length, (2.) subreflector diameter and surface shape (some improvement may be realized by slight modification of the hyperboloid), (3.) feed-horn aperture and taper, and (4.) TE_{11} to TM_{11} mode conversion.

Converting a certain portion of dominant mode in the horn to the higher-order TM_{11} mode broadens the subreflector illumination and controls the spillover at the same time.[1]

III. ANTENNA GEOMETRY

3.1 *Introduction*

The open cassegrain feed horn propagates both TE_{11} and TM_{11} modes. By suitable choice of mode amplitude ratio and relative phase a nearly circular radiation pattern can be obtained. The horn then radiates a nearly spherical wave front originating from a point designated as the phase center, which determines the location for one of the focal points of the subreflector hyperboloid. Based on geometrical optics the hyperboloid surface reflects the incident spherical wave as a wave effectively originating from the other focal point of the hyperboloid. In the open cassegrain, the latter focus coincides with that of the paraboloid surface of which the main reflector is an offset elliptic section. The main reflector converts the reflected spherical wave to a plane wave in the antenna aperture.

Several related coordinate systems were used for the antenna analysis, and a number of useful relationships were derived. Two sets of rectilinear coordinates are basic: x_p, y and z_p with origin at the paraboloid focus and z_p lying along the axis of revolution as shown in Fig. 3, and x_s, y, z_s with the same origin but rotated so that z_s coincides with the secondary optics axis as shown in Fig. 4. These will be called the primary and secondary coordinate systems, respectively.

A spherical system is classically related to each of these rectilinear systems with poles on the z axis, θ measured from the $+z$ axis and φ measured counterclockwise from the x-z plane. y and r are common and carry no subscript. Certain convenient auxiliary coordinates are also used.

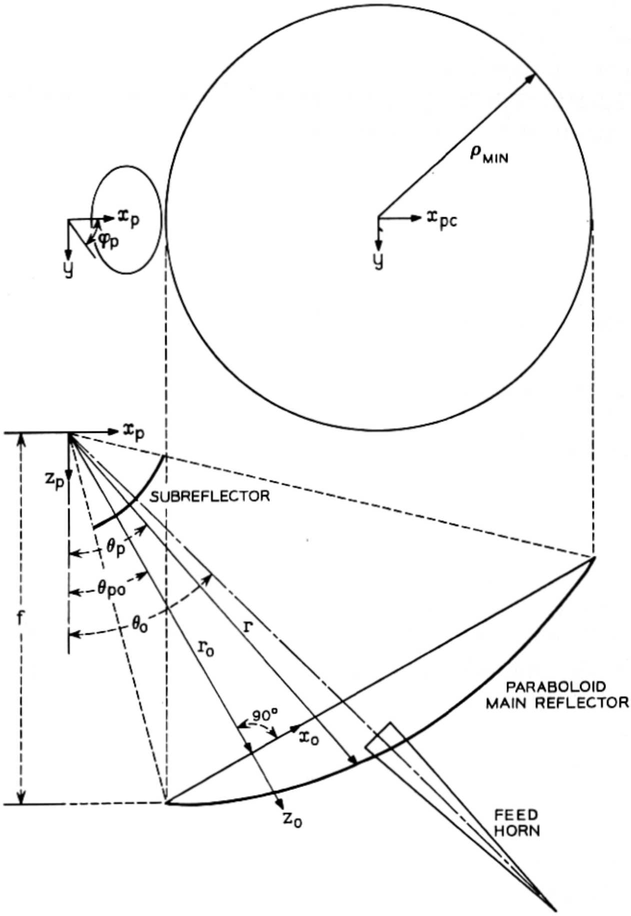

Fig. 3 — Antenna primary coordinates.

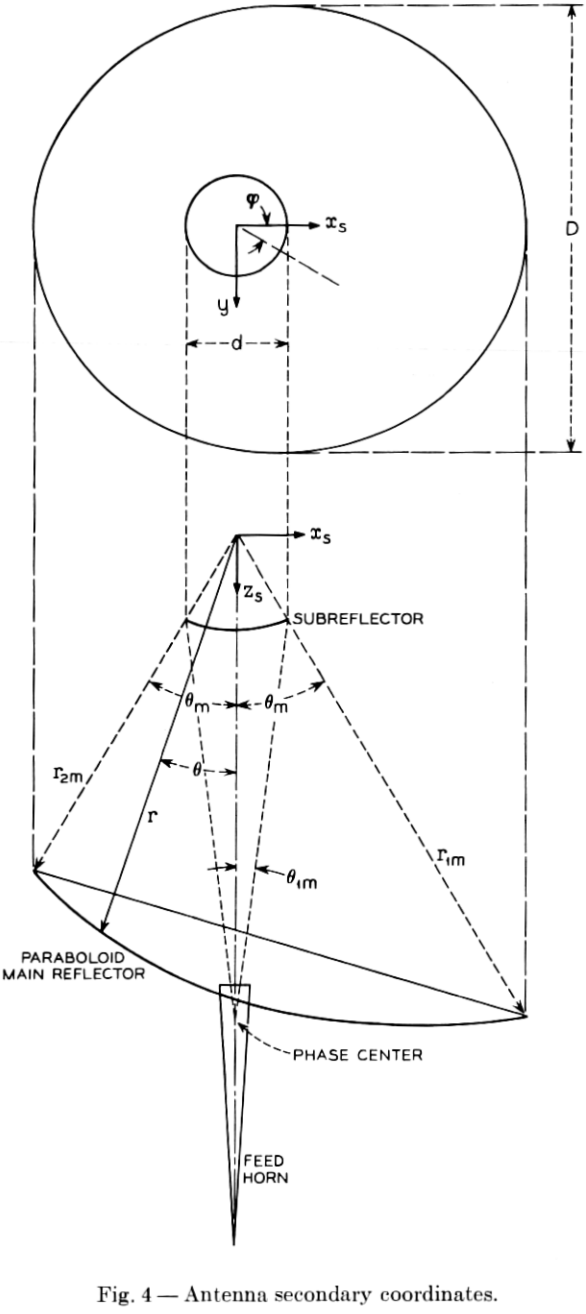

Fig. 4 — Antenna secondary coordinates.

3.2 *Paraboloid Reflector*

The paraboloid reflector is a section of a paraboloid of revolution about the z_p axis of focal length f. The equation for the paraboloid in primary spherical coordinates (aligned with the x_p, y, z_p coordinates) is:

$$r = \frac{2f}{1 + \cos \theta_p}. \tag{1}$$

In secondary spherical coordinates (aligned with the x_s, y, z_s coordinate system as shown in Fig. 4), the equation for the paraboloid surface is:

$$r = \frac{2f}{1 + \cos \theta \cos \theta_0 - \sin \theta \sin \theta_0 \cos \varphi}. \tag{2}$$

(The subscripts have been dropped from θ and φ secondary spherical coordinates for convenience.)

The curves of intersection of the paraboloid surface with cones, $\theta = \theta_c$, (constant) are ellipses and lie in planes perpendicular to the x_p, z_p plane. (Equations for the ellipses are presented in Appendix A.) The projections of these intersections onto the x_p, y plane are circles given by:

$$\left(x_p - \frac{2f \sin \theta_0}{\cos \theta_c + \cos \theta_0}\right)^2 + y^2 = 4f^2 \left(\frac{\sin \theta_c}{\cos \theta_c + \cos \theta_0}\right)^2. \tag{3}$$

The projections of the intersections of the planes $\varphi = \varphi_c$ with the paraboloid are also circular arcs given by:

$$(x + 2f \cot \theta_0)^2 + \left(y - \frac{2f \cot \varphi_c}{\sin \theta_0}\right)^2 = \frac{4f^2}{\sin^2 \theta_0 \sin^2 \varphi_c}. \tag{4}$$

The two sets of circles (3) and (4) are shown in Fig. 5 for $\theta_0 = 47.5°$. The sets of circles (3) and (4) are orthogonal; the projections of the intersection are therefore conformal. The special case, $\theta_0 = 90°$, corresponds to the projections of the horn-reflector antenna previously obtained by T. Li.[5]

3.3 *Hyperboloid Subreflector*

Referring to Fig. 6, the equation for the hyperboloid surface is given by the relationship:

$$|r_1| - |r_2| = b \tag{5}$$

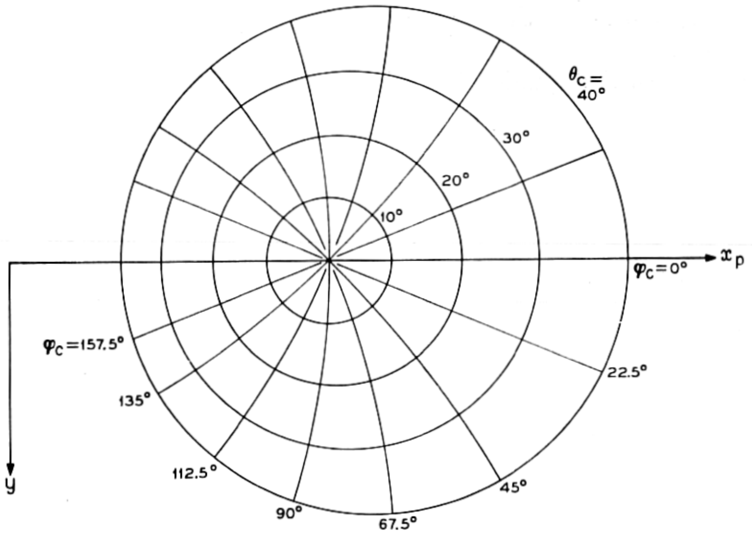

Fig. 5 — Projection circles of the paraboloid reflector.

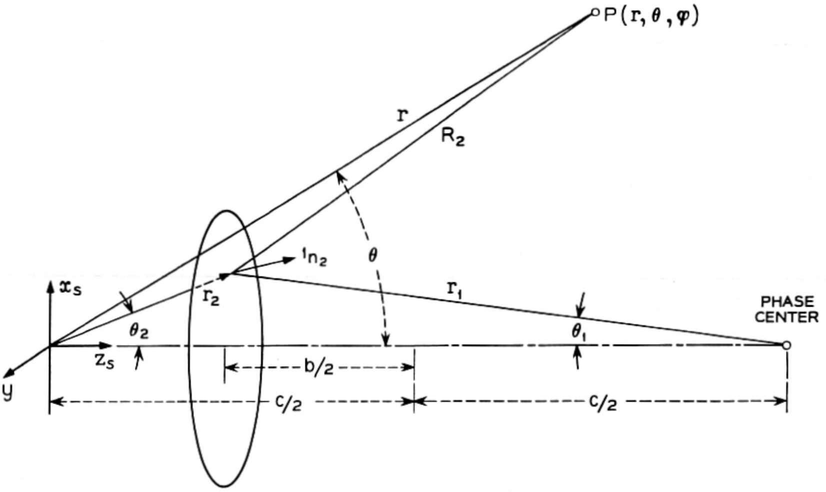

Fig. 6 — Subreflector coordinates.

where r_1 and r_2 are the distances from the foci and b is an arbitrary constant.

From (5), the equation for the hyperboloid surface in terms of θ_1 is:

$$r_1 = \frac{c}{2} \cdot \frac{(1 - \beta^2)}{\cos \theta_1 - \beta} \tag{6}$$

where

c = distance between the foci of the hyperboloid

and

$$\beta = b/c. \tag{7}$$

Similarly, in terms of θ_2,

$$r_2 = \frac{c}{2} \cdot \frac{(1 - \beta^2)}{\beta + \cos \theta_2}. \tag{8}$$

The relations between the angles θ_1 and θ_2 are

$$\cos \theta_1 = \frac{(1 + \beta^2) \cos \theta_2 + 2\beta}{1 + \beta^2 + 2\beta \cos \theta_2} \tag{9}$$

and

$$\cos \theta_2 = \frac{(1 + \beta^2) \cos \theta_1 - 2\beta}{1 + \beta^2 - 2\beta \cos \theta_1}. \tag{10}$$

The representation of the hyperboloid surface in the two coordinate systems is useful for the computations of the radiation patterns from the horn and subreflector.

3.4 *Relations Between the Antenna Parameters*

From the antenna geometry, and the restriction that the subreflector must not block the aperture, certain relationships between the antenna parameters can be established.

The relationship between the diameter D of the projected circle of the paraboloid surface in the x_p, y plane, the geometrical illumination angle θ_m, and the focal length of the paraboloid f is:

$$\sin \theta_m = \frac{\tau[\cos \theta_0 + \sqrt{1 + \tau_2 \sin^2 \theta_0}]}{1 + \tau^2} \tag{11}$$

with

$$\tau = D/4f. \tag{12}$$

The relationship between the diameter d, of the hyperboloid, and the diameter of the projected circle is:

$$\frac{d}{D} = \frac{\sin(\theta_0 - \theta_m)\sin\theta_m}{\tau[1 + \cos(\theta_0 - \theta_m)]\sin(\theta_0 + \theta_m)}. \tag{13}$$

The angle θ_{0m} subtended by the hyperboloid reflector at the intersection of the feed horn axis and paraboloid is:

$$\tan\theta_{0m} = \frac{\tau(1 + \cos\theta_0)\tan\theta_m}{\frac{D}{d}\tan\theta_m - \tau(1 + \cos\theta_0)}. \tag{14}$$

The ratio of minimum to maximum distance from the focal point of the paraboloid to the elliptical main reflector surface is:

$$\frac{r_{2m}}{r_{1m}} = \frac{1 + \cos(\theta_0 + \theta_m)}{1 + \cos(\theta_0 - \theta_m)}. \tag{15}$$

The relations (11), (13)–(15) are shown in Fig. 7 as a function of $D/4f$ for $\theta_0 = 47.5°$.

3.5 *The Antenna Dimensions*

The antenna gain is closely related to the diameter D, of the projected circle of the paraboloid reflector. For a specified antenna gain and assuming a reasonable aperture efficiency (60–70 per cent) the diameter D is also specified.

It is evident from Fig. 7 that a large focal length paraboloid for a specified D (i.e., τ small) has several advantages. By using a larger f, a larger subreflector can be used without introducing aperture blocking. The angle θ_{0m} subtended by the subreflector is larger and hence a smaller horn aperture can be used to illuminate the subreflector. Also, a large subreflector will produce less radiation beyond the geometrical illumination angle and hence less spillover at the main reflector. On the other hand, a large subreflector is difficult to support mechanically.

The aperture of the horn feed should be as small as possible to avoid blocking of the main reflector area, but large enough to provide efficient illumination of the subreflector. A uniform phase (plane phase front) aperture feed would be most suitable since it provides the minimum beamwidth for a given aperture size. Such an aperture is not readily realizable without the use of lenses, but a narrow angle horn provides a suitable alternative. The choice of the horn length and position was also influenced by mechanical considerations. The final horn dimensions were selected by computing the radiation patterns from a horn of fixed length and different angles, and maximizing the power intercepted by the subreflector.

The antenna dimensions are:

Paraboloid offset angle	$\theta_0 = 47.5°$
Focal length of paraboloid	$f = 152\lambda$
Diameter of the subreflector	$d = 40\lambda$
Horn length	$l = 100\lambda$
Horn angle	$\alpha = 3.25°$
Main reflector geometrical illumination angle	$\theta_m = 30.5°$
Subreflector geometrical illumination angle	$\theta_{1m} = 7.5°$.

The above dimensions and the location of the feed horn phase center which is 88.85λ from the vertex of the horn completely specify the antenna geometry.

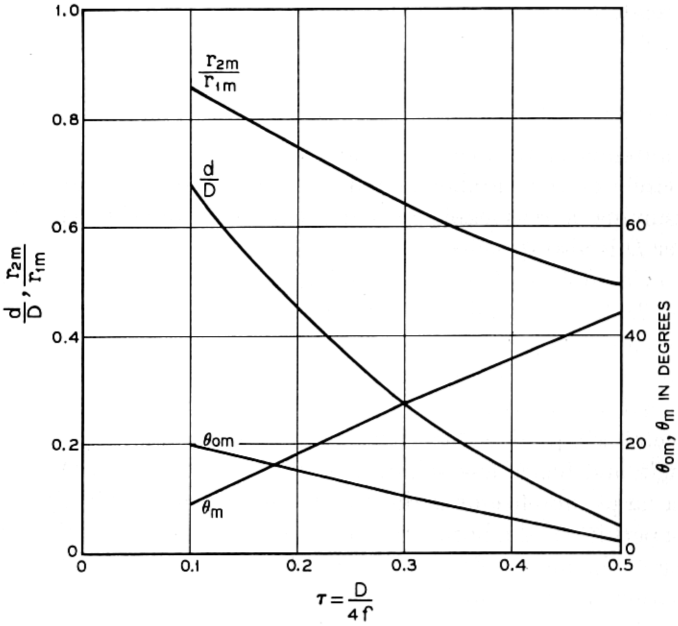

Fig. 7 — Antenna parameters.

IV. RADIATION PATTERN COMPUTATIONS

4.1 *Horn Radiated Pattern*

4.1.1 *Radiation Integrals*

The objectives of the horn pattern computations were: (1.) to determine the phase center and phase front of the radiation pattern, (2.) to optimize the horn angle for a specified horn length for maximum power interception by the subreflector, and (3.) to determine the TM_{11} to TE_{11} mode ratio for phase equalization of the radiation pattern in the two principal planes.

The radiation pattern from the horn has been computed by using the Kirckhoff approximation to the aperture radiation. Based on the above, the electric field, $\bar{E}_p$, at a distance of at least a few wavelengths from the aperture is:[6]

$$\bar{E}_p = \frac{jk}{4\pi} \int_s \int [\bar{E}_a(1 + 1_n \cdot 1_R) - \bar{E}_a \cdot 1_R(1_n + 1_R)] \frac{e^{-jkR}}{R} \, ds \qquad (16)$$

where

s = horn aperture area
$k = 2\pi/\lambda$ = propagation constant
λ = wavelength

and 1_n and 1_R are unit vectors in the normal and R direction respectively as shown in Fig. 8. $\bar{E}_a$ is the field in the horn aperture, assumed to be the

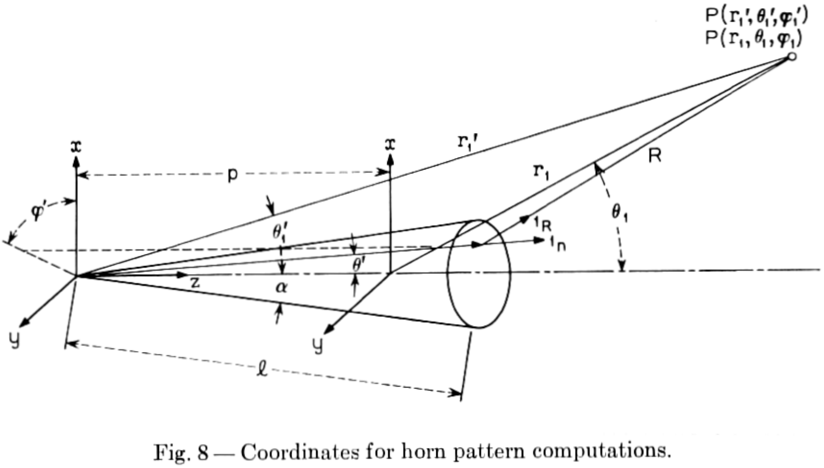

Fig. 8 — Coordinates for horn pattern computations.

same as for circular waveguide propagating TE_{11} and TM_{11} modes, but with spherical phase fronts.

The aperture field $\bar{E}_a$ has both TE_{11} and TM_{11} mode components designated by:

$$\bar{E}_a = \bar{E}_{a\mathrm{TE}} + \bar{E}_{a\mathrm{TM}}. \tag{17}$$

The aperture fields used in the computation are given in Appendix B.

Two different observation coordinate systems have been used to compute the radiation integral (16). The initial computation was performed in the coordinate system θ_1', φ_1' with origin at the vertex of the horn. From this computation, the phase center of the radiation pattern was determined. The subsequent integration was performed in the θ_1, φ_1 coordinate system with origin at the phase center.

Only the first term of the integral (16) has been evaluated, since it has been shown[7] that even for a much wider angle horn than considered here the contribution of the second term is negligible. Furthermore, it is shown in Appendix B that it is sufficient to evaluate (16) for one rectilinear component of one polarization in the two principal planes $\varphi_1 = 0$ and $\varphi_1 = \pi/2$. The other components of the radiation pattern can be derived from that computation.

The following integral has been evaluated in both coordinate systems for the case when the TE_{11} and TM_{11} mode are in phase at the horn aperture.

$$E_{py} = A_y \frac{kl^2}{4\pi} \int_0^{\alpha} \int_0^{2\pi} \left[(E_{ay\mathrm{TE}})_y + \frac{B_y}{A_y} (E_{ay\mathrm{TM}})_y \right] \cdot \frac{e^{-jkR}}{R} (1 + 1_n \cdot 1_R) \sin\theta' \, d\theta' \, d\varphi'. \tag{18}$$

The subscript y indicates that the y components of (68) and (71) have been used.

The resulting radiation patterns for both polarizations are:

$$(\bar{E}_p)_x = 1_{\theta_1} E_{py}(\pi/2) \cos\varphi_1 - 1_{\varphi_1} E_{py}(0) \sin\varphi_1 \tag{19}$$

$$(\bar{E}_p)_y = 1_{\theta_1} E_{py}(\pi/2) \sin\varphi_1 + 1_{\varphi_1} E_{py}(0) \cos\varphi_1 . \tag{20}$$

The explicit φ_1 dependence of the radiation patterns simplifies considerably the subsequent computations of the radiation from the subreflector.

4.1.2 *Phase Centers*

The phase center designates the location of the center of curvature of a spherical surface which is tangential to the equiphase surface near the maximum of the radiation pattern. The phase center is particularly useful when the equiphase surface is nearly spherical over a relatively wide angle. For such a radiation pattern the phase variation is minimized in a spherical coordinate system with its origin at the phase center. The existence of a well-defined phase center depends on the spatial dependence of the equiphase surface. However, through any principal plane of the radiation pattern the radius of curvature at the center of the equiphase curve can be determined. For a circular horn coherently excited in the TE_{11} and TM_{11} modes it is possible to adjust the ratio of the two modes such that the centers of curvature of the radiation in the two principal planes coincide.

The radii of curvature in the two principal planes can be determined from the integral for the radiation pattern (18).[8,9] An alternate method is to compute the radiation pattern of the horn in a spherical coordinate system with its origin at the horn vertex. From the phase variation of the radiation pattern in this coordinate system at a constant radius the radii of curvature can also be determined. The latter method was used here.

Referring to Fig. 8, and assuming that the radiation pattern has a spherical wave front over a certain angular range, the phase dependence, δ, of the electric field will be

$$\delta = -(kr_1 + \delta_0). \tag{21}$$

The phase of the field computed in a coordinate system with its origin at the vertex of the horn

$$\delta = -\left(k\sqrt{(r_1')^2 + p^2 - 2r_1'p\cos\theta_1'} + \delta_0\right). \tag{22}$$

The relative phase, δ_r with respect to the phase at $\theta_1' = 0$ is:

$$\delta_r = -k\left[\sqrt{(r_1')^2 + p^2 - 2r_1'p\cos\theta_1'} - (r_1' - p)\right]. \tag{23}$$

From (23), p can be determined since δ_r is known from the computation:

$$\frac{p}{\lambda} = \frac{\dfrac{\delta_r}{4\pi}\left(2\dfrac{r_1'}{\lambda} - \dfrac{\delta_r}{2\pi}\right)}{\left[\dfrac{\delta_r}{2\pi} - \dfrac{r_1'}{\lambda}(1 - \cos\theta_1')\right]}. \tag{24}$$

From (24) the location of the phase center can be determined as a function of θ_1'. For the horn radiation pattern under consideration p is constant over a wide angular range of θ_1'. The value used for determining p was $\theta_1' = 0.5°$.

The position of the phase center was computed initially for a TE_{11} mode in the H plane. Subsequently, the pattern in the E plane was computed (in the coordinate system with its origin at the *H*-plane phase center) for different ratios of TE_{11} to TM_{11} mode. The TM_{11} mode has little effect on the radiation pattern in the *H* plane (the *H* plane, far-field radiation pattern of an open waveguide is zero), and the location of the *H*-plane phase center was unaffected by variations in the mode ratio. The ratio of the TM_{11} to TE_{11} mode was selected to make the phase dependence in the two principal planes similar. The amplitude and phase of the radiation patterns in the *E* and *H* planes are shown in Fig. 9 for the following parameters:

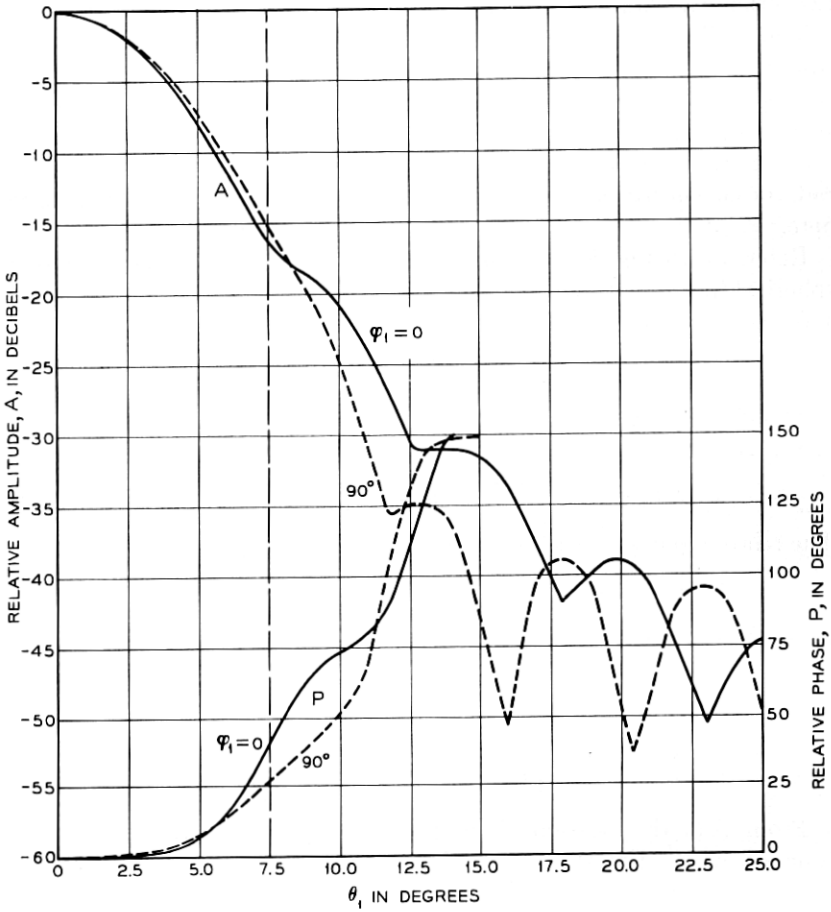

Fig. 9 — Amplitude and phase of feed horn radiation.

$l = 100\lambda$
$\alpha = 3.25°$
TM_{11} to TE_{11} mode ratio $(B_y/A_y) = 0.51$*
$p = 88.85\lambda$
$r = 149.84\lambda$

The subreflector intercepts the power over a 7.5° angle in θ_1. Over this range, the phase deviations are 26° and 39° in the E and H planes, respectively. As subsequently discussed, the subreflector has been compensated for the average phase deviation in the two planes. The power intercepted by the subreflector is 94.5 per cent of the total power radiated by the horn. This value has been obtained by integration of the computed radiation patterns.

4.1.3 *Subreflector Compensation*

The computed radiation pattern from the horn shows that its phase deviates from a spherical wave front. Based on geometrical optics, compensation of the hyperboloid subreflector is necessary to obtain a reflected wave with a spherical wave front. The theorem by Malus states that a surface exists which will convert an incident equiphase surface into a reflected equiphase surface and also satisfy Snell's law of reflection.[6] In Appendix C, a method for the construction of a reflector surface which converts an equiphase surface into a reflected spherical surface is presented. However, for a small phase deviation of the incident wave from a spherical phase front, a simpler method can be used.

Let

$$\Delta\delta_r = (2\pi/\lambda)r - (2\pi/\lambda)r_e \tag{25}$$

where

$\Delta\delta_r$ = phase deviation
r = geometrical distance from the phase center to the hyperboloid surface
r_e = apparent geometrical distance.

The equation for the reflector surface is, from (5),

$$r_e - r_2 = b. \tag{26}$$

Solving for r_2 considering that $\Delta\delta_r$ is small yields:

$$r_2 = r_{2h}(\theta_2) - \frac{\lambda\Delta\delta_r(\theta_2)}{4\pi} \cdot \frac{(1 + \beta^2 + 2\beta\cos\theta_2)}{(\cos\theta_2 + \beta)^2} \tag{27}$$

where $r_{2h}(\theta_2)$ is one equation for the hyperboloid surface given by (8).

---

* The corresponding TM_{11} to TE_{11} power ratio is 0.173.

4.2 *Radiation Patterns from the Subreflector*

To compute the radiation pattern from the subreflector it is necessary to determine the current in the subreflector due to the incident wave from the horn. Without solving an integral equation for the current, it can only be determined approximately. A good approximation for subreflectors large in comparison to the wavelength is to assume that the subreflector is locally plane. With the above assumption, and the assumption that the interaction of the feed with the subreflector is negligible, the surface current density $\bar{J}$ at the subreflector is:[6]

$$\bar{J} = \frac{2}{\eta} 1_n \times (1_{\pi_i} \times \bar{E}_i) = \frac{2}{\eta} 1_n \times (1_{\pi_r} \times \bar{E}_r) \tag{28}$$

where

1_n = unit normal to the subreflector surface
$1_{\pi_i}, 1_{\pi_r}$ = directions of propagation for the incident and reflected waves, respectively
$\bar{E}_i, \bar{E}_r$ = incident and reflected electric fields, respectively.

The reflected field is related to the incident field by

$$\bar{E}_r = -\bar{E}_i + 2(1_n \bar{E}_i \cdot 1_n) . \tag{29}$$

It is preferable to express the current density in secondary spherical coordinates due to the subsequent integration which will be performed to obtain the subreflector radiation pattern.

For a hyperboloid or compensated hyperboloid subreflector

$$1_{\pi_r} = 1_{r_2} \tag{30}$$

and

$$1_{n_2} = \frac{1_{r_2}(\cos\theta_2 + \beta) - 1_{\theta_2}\sin\theta_2}{\sqrt{1 + \beta^2 + 2\beta\cos\theta_2}} . \tag{31}$$

For an incident field given by (19) or (20) namely

$$\bar{E}_i = 1_{\varphi_1} E_{\varphi_1} + 1_{\theta_1} E_{\theta_1} . \tag{32}$$

It follows that

$$\bar{E}_r = -1_{\varphi_2} E_{\varphi_1} - 1_{\theta_2} E_{\theta_1} . \tag{33}$$

The radiated electric field, $\bar{E}_s$ from the subreflector due to the current distributions (28) is, with reference to Fig. 6,

$$\bar{E}_s = \frac{j}{\lambda} \int_0^{\theta_m} \int_0^{2\pi} 1_{R_2} \times \left[\left(\bar{E}_r - \frac{1_{r_2} 1_{n_2} \cdot \bar{E}_r}{1_{n_2} \cdot 1_{r_2}} \right) \times 1_{R_2} \right] \frac{e^{-jk(R_2+r_2)}}{R_2} r_2^2 \sin \theta_2 \, d\theta_2 \, d\varphi_2 \tag{34}$$

In (34), E_r represents the amplitudes of the reflected field components. The first term in the brackets of the equation is similar to the Kirckhoff approximation to the radiation from apertures; the second term is due to the radial subreflector currents.

In the computation of the radiation patterns 1_{R_2} has been approximated by 1_r. An actual computation showed that in the principal planes this approximation has a negligible effect on the radiation patterns.

The θ and φ component of radiated field from the subreflector with the above assumption is:

$$\bar{E}_s \cdot 1_{\theta,\varphi} = \frac{-j\eta}{2\pi} \int_0^{2\pi} \int_0^{\theta_m} \bar{J} \cdot 1_{\theta,\varphi} \frac{e^{-jk(R_2+r_2)}}{R_2} \frac{r_2^2 \sin \theta_2}{1_{n_2} \cdot 1_{r_2}} \, d\theta_2 \, d\varphi_2 . \tag{35}$$

From (28)–(33)

$$\begin{aligned} \bar{J} \cdot 1_\theta = {} & \frac{2}{\eta\sqrt{1 + \beta_2 + 2\beta \cos \theta_2}} \{ E_{\theta_1} [\cos \theta \cos (\varphi_2 - \varphi) \\ & \cdot (1 + \beta \cos \theta_2) + \beta \sin \theta \sin \theta_2] \\ & - E_{\varphi_1} \cos \theta \sin (\varphi_2 - \varphi) (\cos \theta_2 + \beta) \} \end{aligned} \tag{36}$$

and

$$\begin{aligned} \bar{J} \cdot 1_\varphi = {} & \frac{2}{\eta\sqrt{1 + \beta^2 + 2\beta \cos \theta_2}} \{ E_{\theta_1} \sin (\varphi_2 - \varphi)(1 + \beta \cos \theta_2) \\ & + E_{\varphi_1} \cos (\varphi_2 - \varphi) (\cos \theta_2 + \beta) \}. \end{aligned} \tag{37}$$

The distance R_2 is

$$R_2 = \sqrt{r^2 + r_2^2 - 2rr_2 \cos \gamma_2} \tag{38}$$

with

$$\cos \gamma_2 = \sin \theta \sin \theta_2 \cos (\varphi - \varphi_2) + \cos \theta \cos \theta_2 . \tag{39}$$

The φ_2 dependence of E_{θ_1} and E_{φ_1} for x and y polarization is given by (19) and (20) respectively with $\varphi_1 = \varphi_2$.

It is sufficient to evaluate (34) for one polarization only in the two principal planes $\varphi = 0$ and $\varphi = \pi/2$, to obtain the φ dependence of the radiation pattern on a spherical surface centered about the focal point of the hyperboloid. Furthermore, for y polarization, the φ component of (35) may be evaluated at $\varphi = 0$ and the θ component at $\varphi = \pi/2$. The φ dependence of the radiation pattern is the same as for the horn (19) and (20).

The φ and θ components of the electric field radiated by the subreflector, due to an incident field polarized in the y direction has been computed in the H and E plane, respectively. Figs. 10 and 11 show the amplitude and phase of the radiation pattern in the H plane. Values are shown along a circle whose center is at the focus of the hyperboloid and which passes through the intersection of the subreflector axis and the main reflector. A sample computation at distances corresponding to the location of the paraboloid surface showed an inverse distance relationship as would be expected from a spherical wave. Fig. 12 shows the E-plane pattern at the location of the paraboloid surface in the illumination region, and at a constant radius in the shadow region corresponding to the radial distance to the edge of the paraboloid reflector. The phase dependence of the E-plane and H-plane patterns are similar.

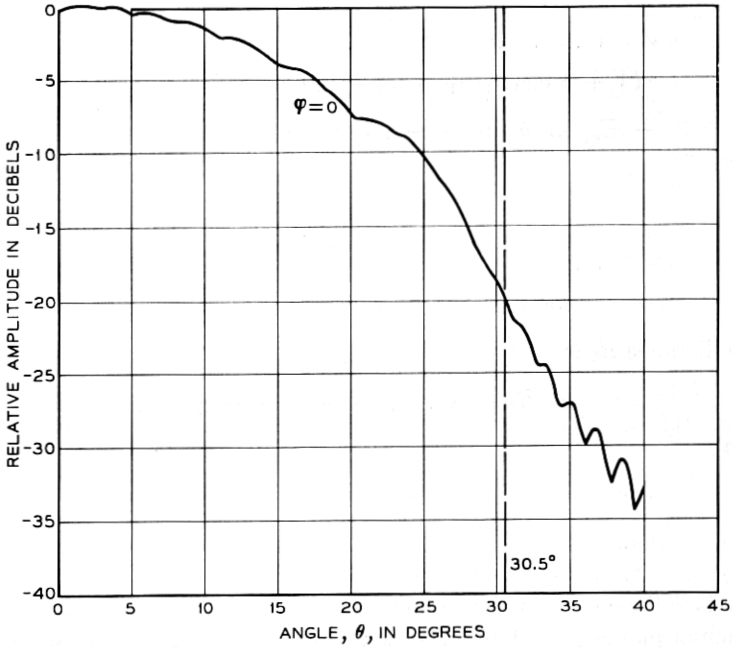

Fig. 10 — Computed subreflector radiation pattern (H plane).

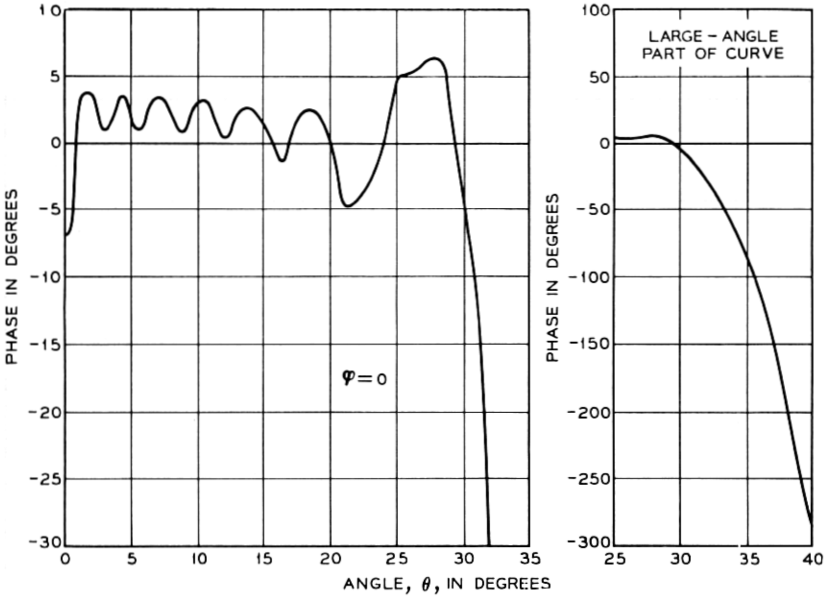

Fig. 11 — Computed phase of subreflector radiation pattern (*H* plane).

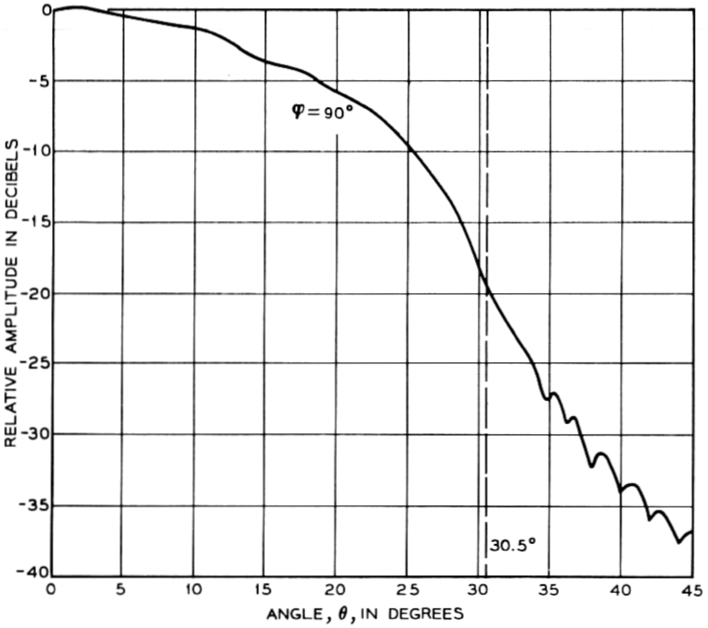

Fig. 12 — Computed subreflector radiation pattern (*E* plane).

There is a distinct difference in radiation patterns in geometrical illumination and shadow regions. In the illumination region the radiation is essentially spherical. In the shadow region (θ larger than 30.5°) the phase varies rapidly, and amplitude variations also occur.

The pattern outside the geometrical illumination region is of utmost interest since it largely determines the antenna noise temperature. The radiated power of the subreflector has been computed as a function of θ by integration of the radiation patterns. The radiated power normalized with respect to the radiated power in angular range 0–45 degrees is shown in Fig. 13 for the $\varphi = 0, \pi/2$ and π radiation patterns. Fig. 13 also shows the antenna noise temperature due to spillover at the main reflector as a function of the angle subtended by the main reflector. The computed antenna noise temperature assumes earth radiation temperature of 300°K.

4.3 *Radiation Pattern from the Main Reflector*

The radiation pattern from the main reflector can be determined by the same method as the radiation pattern from the subreflector. However, the radiation from a paraboloid reflector is primarily determined by the reflected electric field (i.e., the longitudinal currents can be neglected).

The reflected electric field is related to the incident field by (29). The

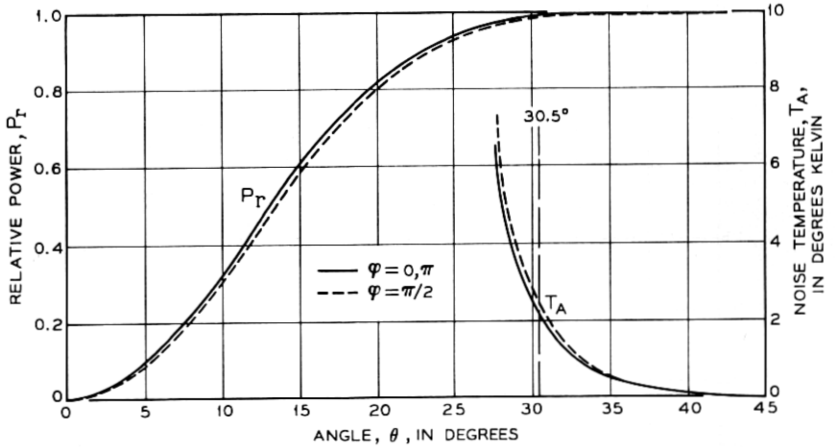

Fig. 13 — Antenna noise temperature and power radiated by the subreflector.

far field of the antenna is given by:

$$\bar{E}_r = \frac{j}{\lambda} \cdot \frac{e^{-jkr_p}}{r_p} \int \bar{E}_{rs} \exp\,[jk \sin\theta_a(x_{pc}\cos\varphi_a + y\sin\varphi_a)]\,ds. \quad (40)$$

The integration is to be performed over the projected area of the paraboloid in the x_p, y plane, and x_{pc} is the coordinate in the x_p direction from the center of the projected circle of the paraboloid. It is preferable to perform the integration in the subreflector coordinate system, since the incident field is already expressed in terms of the secondary coordinate. The vector dependence of the reflected field has to be determined in terms of its components x_p and y. The vector dependence of the reflected field can be obtained from (29), but more directly by noticing the φ and θ components of the incident field transform by reflection into the circles (3) and (4). The unit normal to these circles gives the directions of the reflected θ and φ components respectively. The relationships between the points on the paraboloid surface and their projections onto the x_p, and y plane are

$$x_p = \frac{2f(\cos\theta_0 \sin\theta \cos\varphi + \sin\theta_0 \cos\theta)}{1 + \cos\theta\cos\theta_0 - \sin\theta_0 \sin\theta \cos\varphi} \quad (41)$$

$$y = \frac{2f \sin\theta \sin\varphi}{1 + \cos\theta \cos\theta_0 - \sin\theta \sin\theta_0 \cos\varphi}\,. \quad (42)$$

In terms of x_p and y components, the electric field is:

$$\bar{E}_{rs} = \frac{\left[\begin{array}{l} 1_{xp}\{[\sin\theta_0 \sin\theta - \cos\varphi\,(1 + \cos\theta_0\cos\theta)]E_\theta \\ \qquad + \sin\varphi\,(\cos\theta_0 + \cos\theta)E_\varphi\} \\ - 1_y\{\sin\varphi\,(\cos\theta_0 + \cos\theta)E_\theta \\ \qquad - [\sin\theta\sin\theta_0 - \cos\varphi\,(1 + \cos\theta\cos\theta_0)]E_\varphi\} \end{array}\right]}{1 + \cos\theta_0\cos\theta - \sin\theta_0\sin\theta\cos\varphi} \quad (43)$$

where E_φ and E_θ are the incident components of the electric field at the paraboloid.

It remains to determine the surface element ds in θ, φ coordinates. The surface element can be determined from the Jacobian of (41) and (42). However, a simpler method is available by considering the properties of the paraboloid. The surface element ds is

$$ds = \left(\frac{r^2 \sin\theta\; d\theta\; d\varphi}{1_{np} \cdot 1_r}\right) 1_{np} \cdot 1_{zp} \quad (44)$$

1_{np} = unit normal to the paraboloid surface. But for a paraboloid

$$1_{np} \cdot 1_r = 1_{np} \cdot 1_{zp} \cdot \tag{45}$$

Therefore,

$$ds = r^2 \sin \theta \, d\theta \, d\varphi \tag{46}$$

where r is the equation for the paraboloid (2).

The on-axis antenna gain, G_M, has been computed for y polarization from the relation:

$$G_M = \frac{4\pi}{\lambda^2} \frac{\left| \int_\theta^{2\pi} \int_{\theta_h}^{\theta_m} E_{rsy} \, r^2 \sin \theta \, d\theta \, d\varphi \right|^2}{\int_0^{2\pi} \int_0^{\theta_m} ({E_{rsy}}^2 + {E_{rsx}}^2) \, r^2 \sin \theta \, d\rho} . \tag{47}$$

The angle, θ_h, subtended by the horn at the focal point of the subreflector is 1.9°. (About 2 per cent of the power radiated by the subreflector is incident on the feed horn.)

The aperture efficiency, g, has been obtained from the relation

$$g = G_M / G_0 \tag{48}$$

where G_0 is the gain of a uniformly illuminated aperture.

From (3), G_0 is:

$$G_0 = \left[\frac{4\pi f \sin \theta_m}{\lambda (\cos \theta_m + \cos \theta_0)} \right]^2 . \tag{49}$$

Equation (47) has been evaluated using the computed fields of the subreflector and assuming a uniform phase illumination. The results are tabulated in Table I.

The radiation patterns from the antenna have been computed from (40) for y polarization and for an illumination angle of 30.5°. The patterns in the plane of antenna symmetry, $\varphi_a = 0 (x_p, z_p$ plane), and in the plane perpendicular to the plane of antenna symmetry, $\varphi_a = \pi/2$, are shown in Figs. 14 and 15 together with the measured patterns. Fig. 14 shows also the computed cross-polarized radiation pattern in the plane $\varphi_a = \pi/2$. The cross-polarized component is zero in the plane of antenna symmetry.

TABLE I

ANTENNA GAIN AND APERTURE EFFICIENCY

θ_m	G_M	g
30.5°	54.46 db	70.4%

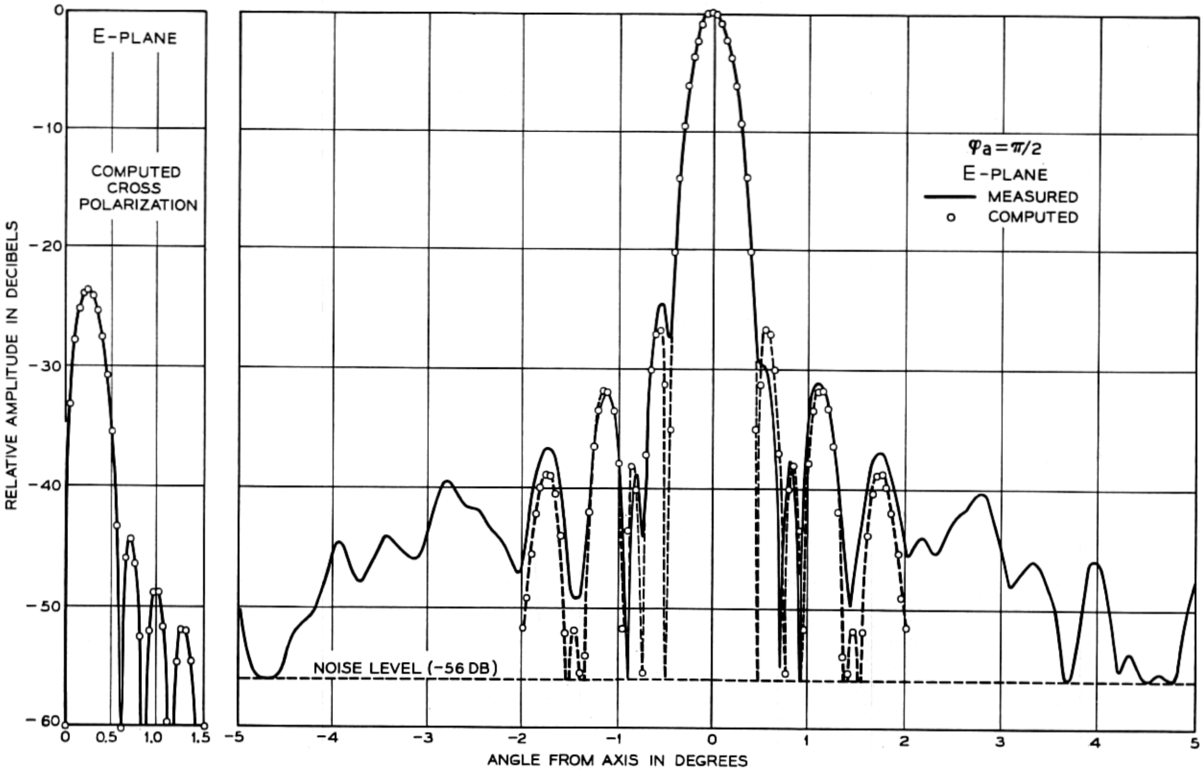

Fig. 14 — Antenna radiation pattern in the plane of asymmetry.

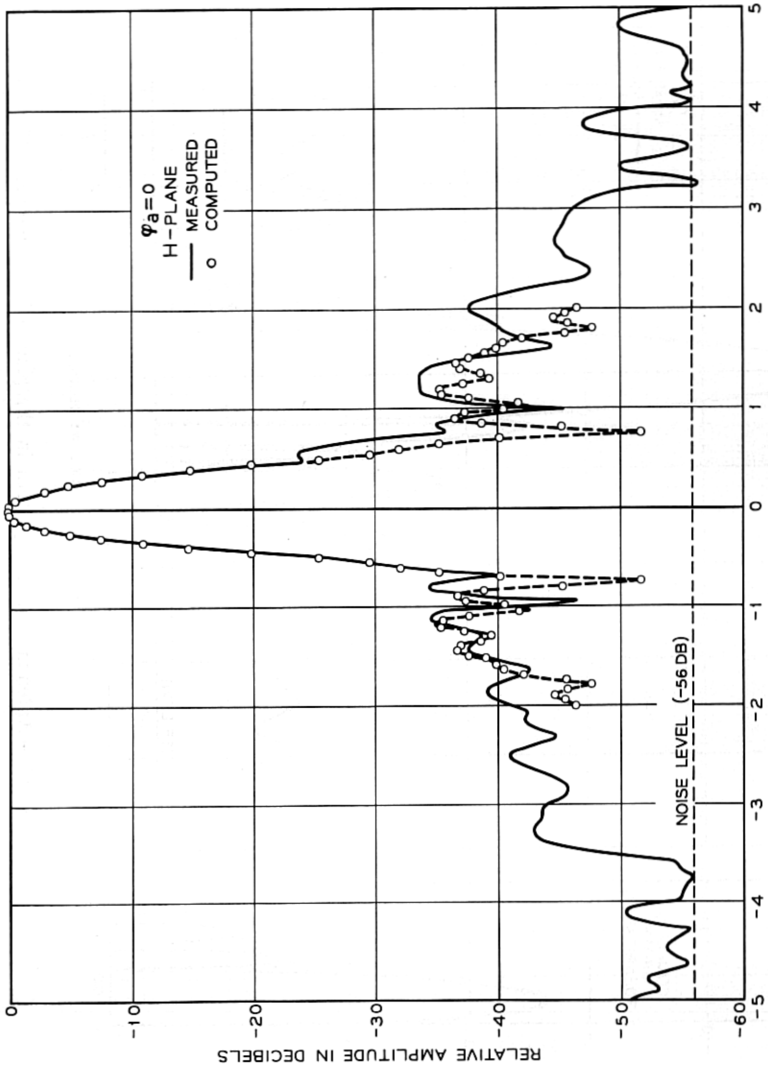

Fig. 15 — Antenna radiation pattern in the plane of symmetry.

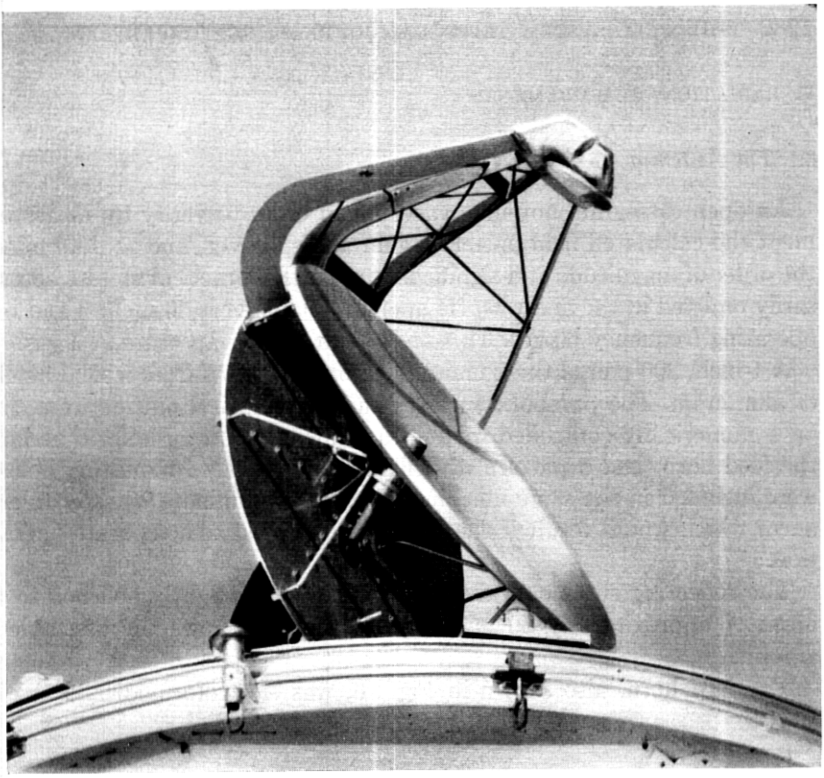

Fig. 16 — Antenna assembly.

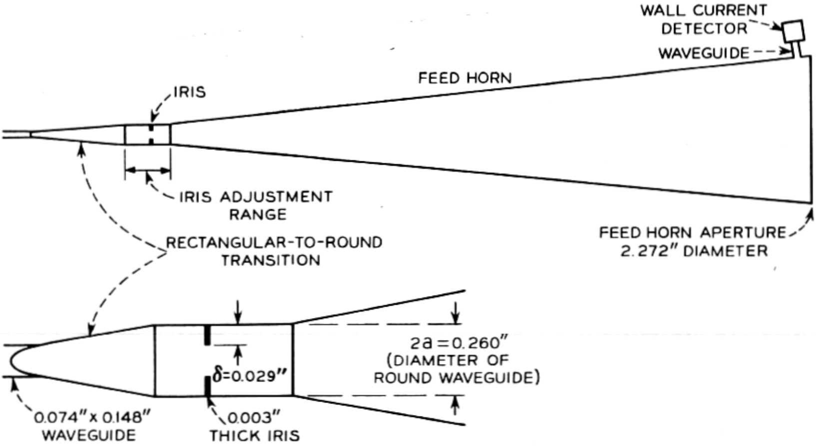

Fig. 17 — Mode converter.

V. RADIATION MEASUREMENTS

5.1 *The Antenna*

An open cassegrain antenna was built in order to verify by measurement the calculated field patterns, gain and spillover, and to determine the order of magnitude and significance of certain practical factors necessarily omitted in the analysis. Its aperture diameter is 40 inches, and its operating frequency 60 gcs. This scales to a 50-foot aperture at 4 gcs.

A 1-inch, 200-pound thick main reflector was milled from a solid block of aluminum. The parabolic surfaces and the elliptical outline were cut on a numerically-controlled milling machine. A slanting hole to accept the feed horn, and a pattern of drilled and spot faced mounting holes, were included in the same machine program to eliminate transfer tolerances which would result if the holes were located as a separate operation.

The reflecting surface of the main reflector was lightly polished to a finish of approximately 50 micro-inches. Fig. 16 shows the assembled antenna.

The feed horn, also shown in Fig. 16, was electroformed, and thick

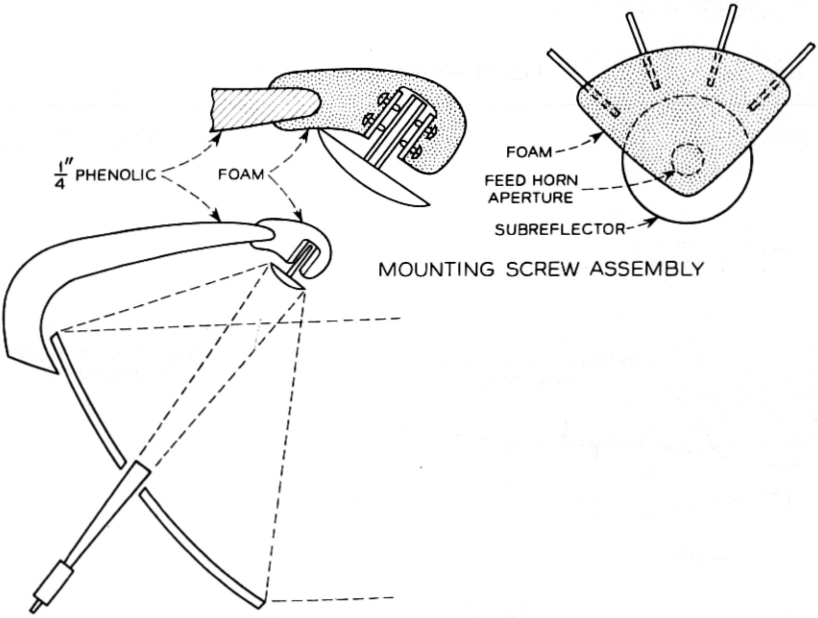

Fig. 18 — Subreflector support.

collars were added so that two sets of adjustable 3-point mounting screws could hold it in place without distorting the horn geometry.

A mode converter was mounted on the small end of the feed horn. The mode converter consists of a single iris chosen to give the required mode conversion when correctly placed with respect to the waveguide transition[2] (Fig. 17). The position of the iris along the horn axis was determined experimentally by monitoring the longitudinal wall current at the horn aperture until a minimum was observed, indicating that the contributions of the TE_{11} and TM_{11} modes were 180° out of phase.

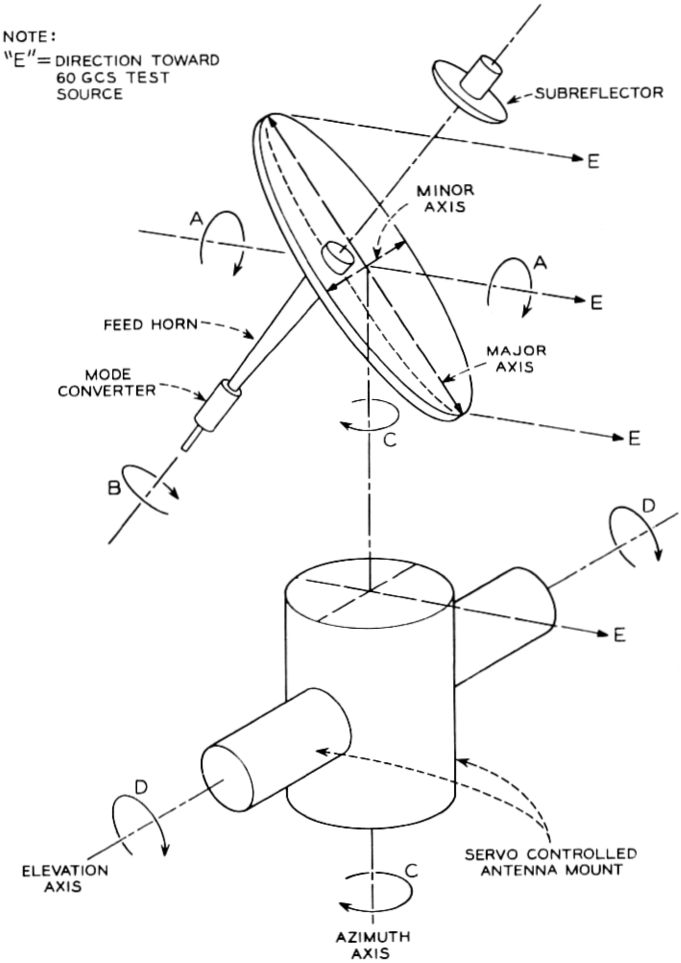

Fig. 19 — Antenna test mount.

The subreflector was turned from an aluminum disc, and as a convenient means of adjusting it, a stem was attached to its rear surface as shown in Fig. 18.

A framework of four $\frac{1}{4}$-inch thick legs of cotton fabric-filled phenolic material was attached to the rear surface of the main reflector. The small ends of the phenolic legs were then jointed together and to the subreflector mounting screw assembly by a block of polyurethane (isocyanate) foam. To eliminate the need for clamps and fasteners, the polyurethane was foamed in place around the items to be joined and supported. The phenolic legs stop short of the edge of the subreflector so that spillover radiation "sees" only the polyurethane foam as shown in Fig. 18.

5.2 *Mounting*

For convenience in electrical testing, the antenna was mounted on a stand which has a horizontal bearing oriented axially with the main beam. The complete antenna can be rotated by hand to any position around this axis "*A*" (Fig. 19), so that the subreflector may be located above, below, or at either side of the main reflector when viewed from the far field source.

The feed horn and mode converter assembly may be rotated by hand (with respect to the rest of the antenna) around its own axis "*B*".

Positioning around axes "*A*" and "*B*" permits *E*-plane and *H*-plane patterns to be measured in any geometrical plane of the antenna.

The stand supporting the antenna was erected on a two-axis servo-

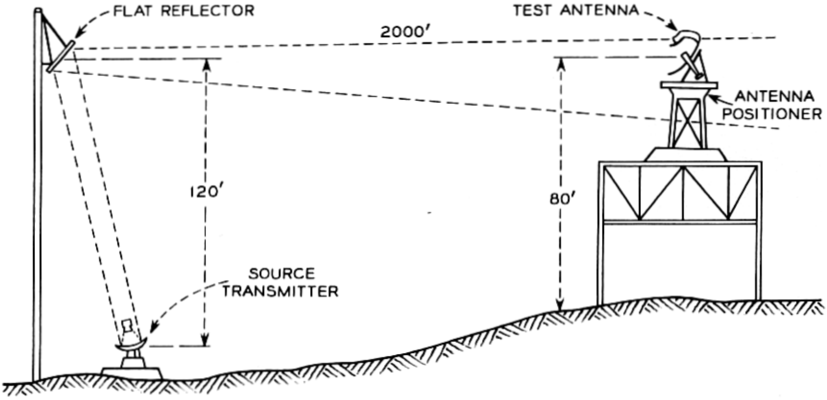

Fig. 20 — Antenna test range.

controlled antenna mount, with vertical axis "*C*" and a horizontal axis "*D*" (Fig. 19). The antenna was located with the intersection of the major and minor axes of the main reflector ellipse intersecting the mount vertical axis "*C*", so that the geometrical center of the main reflector remains stationary when the mount rotates in azimuth. All patterns were measured in the horizontal plane.

5.3 *Range Facility*

The test range configuration is shown in Fig. 20. The field incident on the aperture of the antenna is relatively flat, maximum at the center and between 0.10 and 0.15 db lower around the periphery.

The top of the source tower was stabilized by a long, trussed crossarm and guy wires, limiting movement of the flat, inclined reflector. In a 15-mph wind, the field amplitude variation at the test antenna aperture is approximately 0.1 db, and with 5-to 10-mph winds amplitude variations are not readily detectable.

5.4 *Patterns*

Patterns were measured with the complete antenna installed on the antenna mount of the 2000-foot range facility. *E*-plane and *H*-plane patterns are shown in Figs. 14 and 15.

5.5 *Short-Range Test Facility*

For measuring characteristics of the feed horn with its mode converter, and for measuring the subreflector pattern, a short-range test facility was established. Principal components of the facility are an azimuth antenna positioner (turntable) and three pedestals of rigid polystyrene foam, any one of which may be mounted on the turntable. The three foam pedestals support the feed horn with its mode converter, the subreflector, and either an 8-db or a 16-db pickup horn for sampling the fields.

5.5.1 *Feed Horn Patterns*

A polystyrene foam pedestal supporting the feed horn, with its attached mode converter, was mounted on the azimuth turntable. The feed horn was positioned so that its phase center was located on the vertical axis of rotation of the turntable (see Fig. 21).

For measurement of the patterns, a pickup horn with a $\frac{3}{16}$-inch square

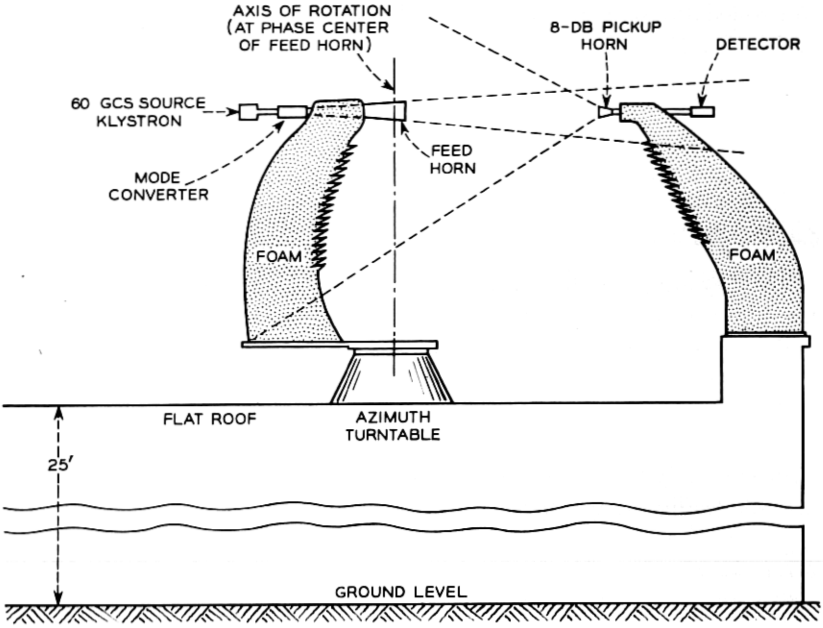

Fig. 21 — Test range for horn radiation measurements.

aperture was designed and fabricated. This horn met the following requirements:

(1.) Directivity was adequate so that no side reflections were detected.

(2.) Deviations of phase or amplitude in the field pattern of the feed horn are small over the angle (approximately 0.35 degrees) intercepted by the $\frac{3}{16}$-inch aperture of the pickup horn.

(3.) With the 100-milliwatt source, and the particular detecting and recording equipment used, the gain of the pickup horn (of the order of 8 db) resulted in a dynamic range, or maximum signal-to-noise ratio, of greater than 55 db.

Figs. 22 and 23 are the E-plane and H-plane measured patterns of the feed horn.

5.5.2 *Subreflector Patterns*

The feed horn with its mode converter was mounted on a polystyrene foam pedestal, and the subreflector was mounted on a second foam pedestal. A pickup horn, supported by a third foam pedestal, was mounted on the azimuth turntable (Fig. 24). The subreflector was located so that its focal point was on the vertical axis of rotation of the turntable.

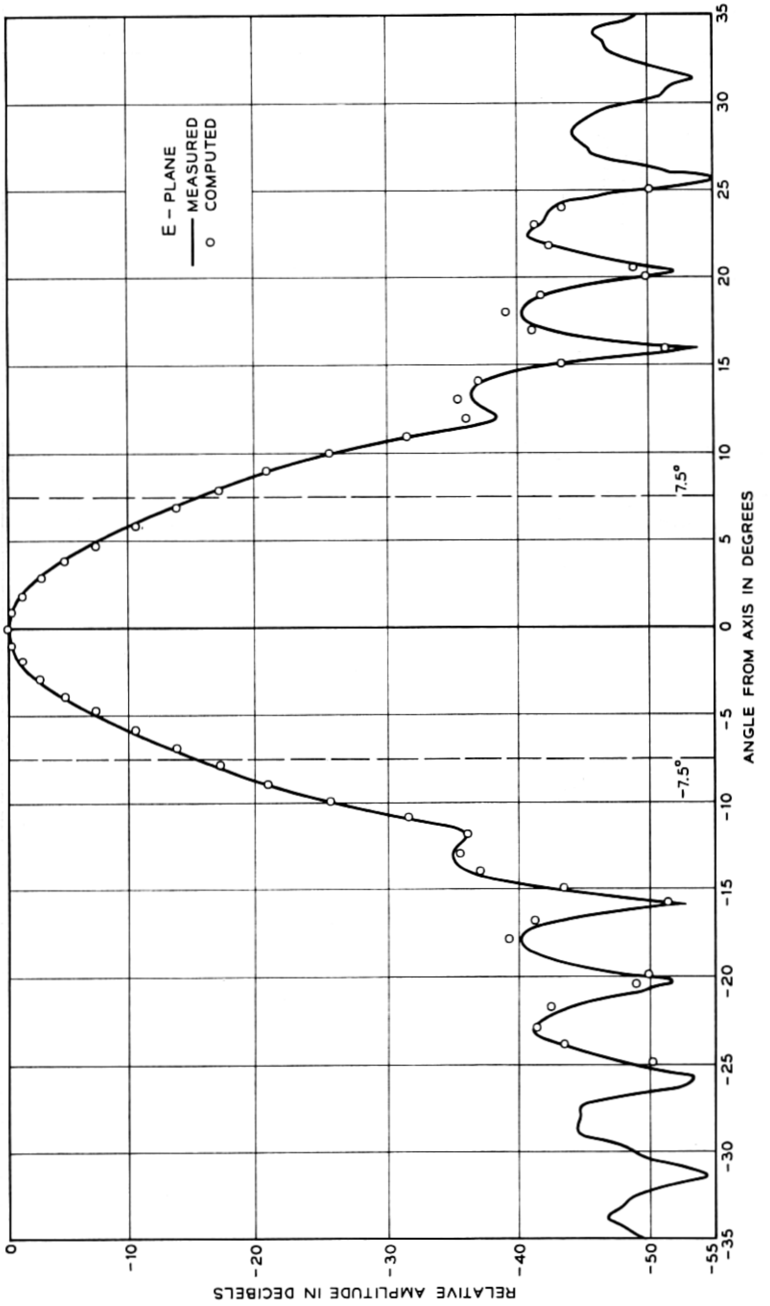

Fig. 22 — *E*-plane radiation pattern of feed horn.

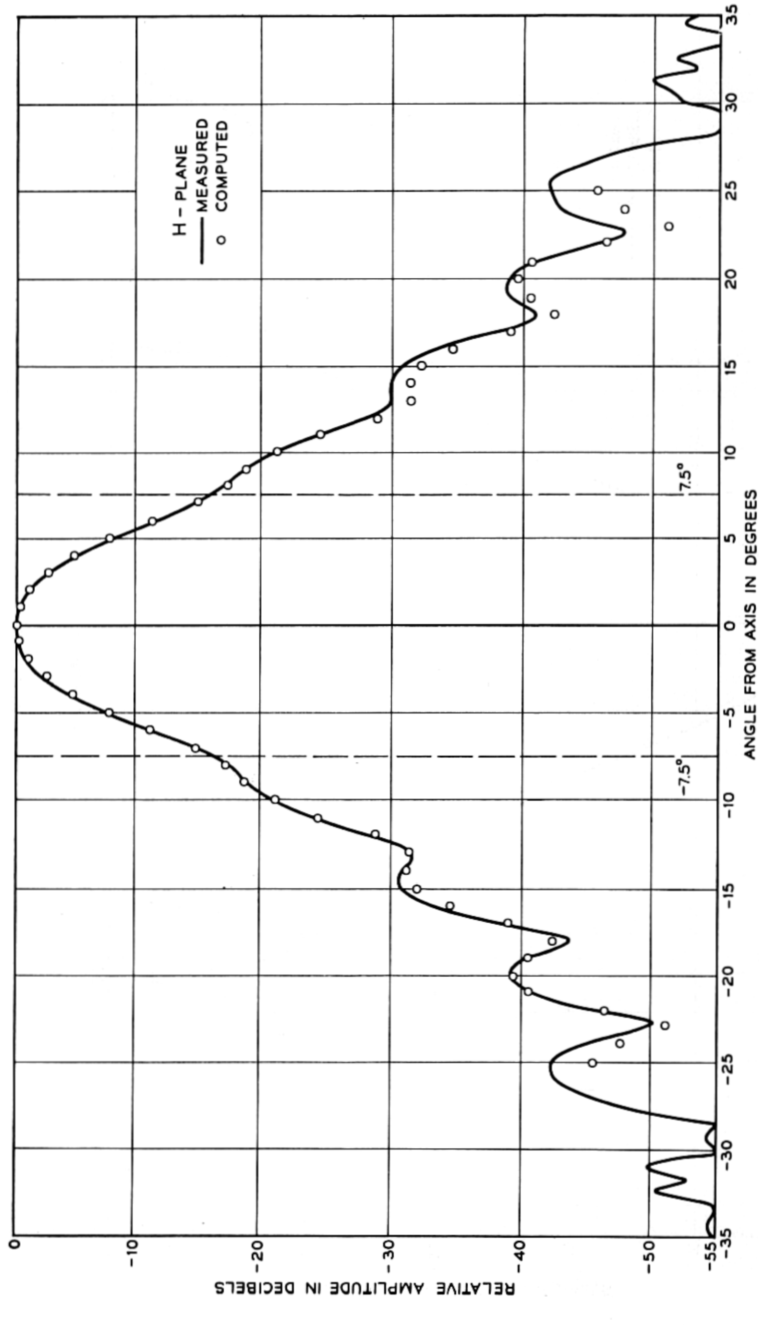

Fig. 23 — *H*-plane radiation pattern of feed horn.

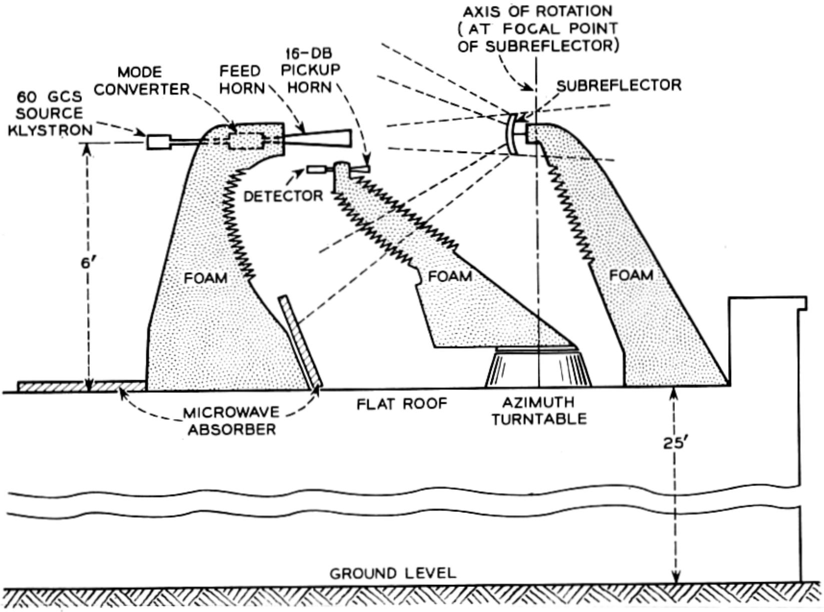

Fig. 24 — Test range for subreflector radiation measurements.

For the subreflector patterns, a 16-db horn was designed and fabricated, meeting requirements of directivity, gain, and pattern resolution somewhat more stringent than those for the feed-horn pattern measurements. In order to gain a little more dynamic range, a 500-milliwatt klystron was used as a 60-gcs source.

Because of the geometry of the antenna, the distance from the subreflector focus to different parts of the main reflector varies. Several subreflector patterns were made at different distances from the focus of the subreflector. The E- and H-plane patterns shown in Figs. 25 and 26 were taken at the distance corresponding to the intersection of the main reflector with the subreflector axis. Patterns at other distances were similar.

For clarity of illustration, Fig. 24 shows the pickup horn located directly below the feed horn. Actually, the feed horn-subreflector axis lies in the plane in which the pickup horn is rotated. Thus, at the closest distance to the subreflector focus, the pickup horn can rotate in front of the feed horn. At the other distances, the pickup horn is stopped short of boresight by 2 or 3 degrees. This missing portion of the center of the pattern is of little consequence, since it is intercepted by the aperture of the feed horn, and does not strike the main reflector.

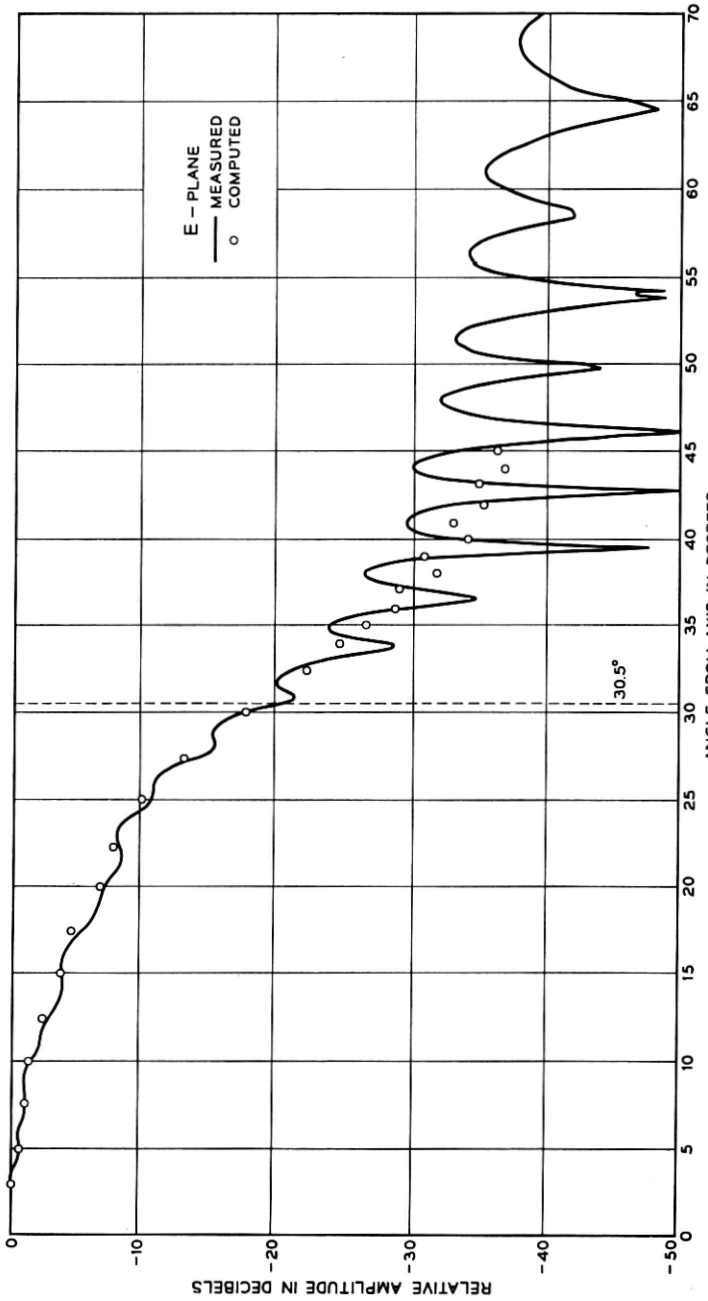

Fig. 25 — *E*-plane radiation pattern of subreflector.

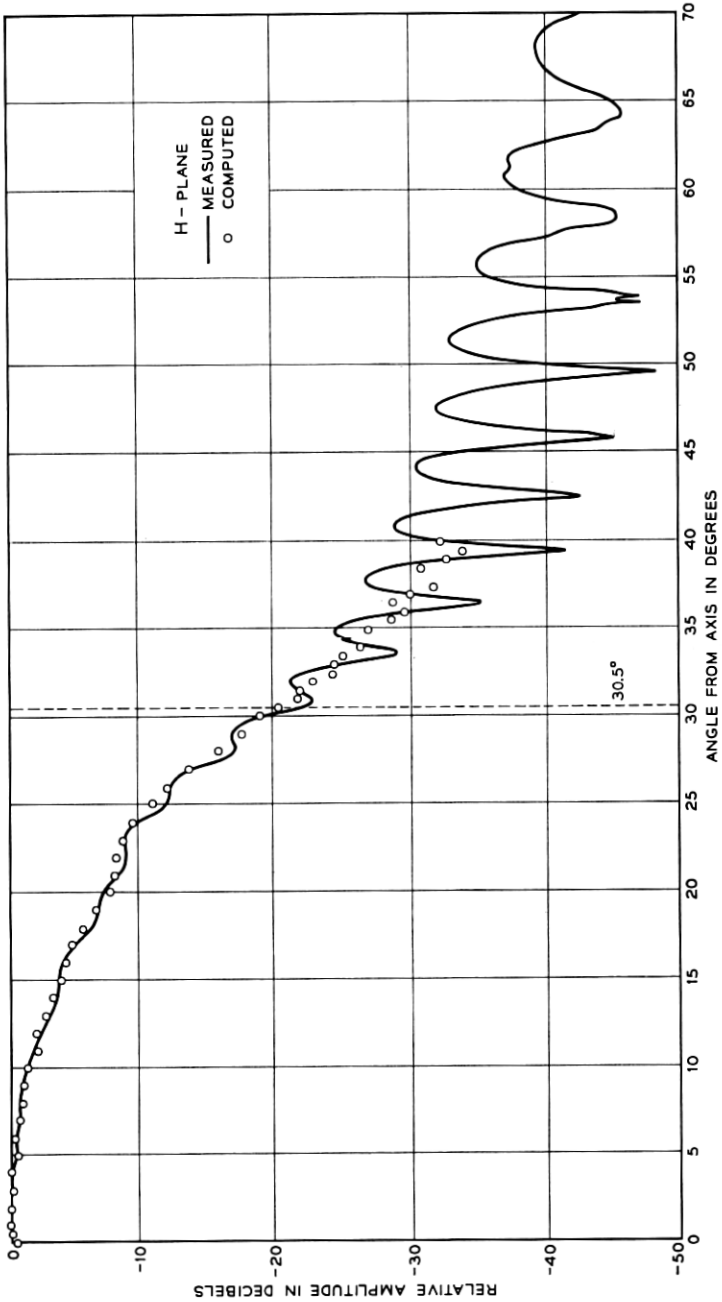

Fig. 26 — *H*-plane radiation pattern of subreflector.

5.6 *Comparison Between the Computed and Measured Radiation Patterns*

Very good agreement has been obtained between the computed and measured patterns of the feed horn. The slight asymmetry in the measured patterns has been demonstrated to be caused by eccentricity of the mode converter.

A comparison between the computed and a measured subreflector pattern is shown in Figs. 25 and 26. Good agreement has been obtained in the geometrical illumination region. In the shadow region the amplitudes and periodicity of the measured side lobes deviate somewhat from the calculated ones. Possible causes for the deviations are:

(1.) The computation is based on an approximate current distribution and does not include edge effects.

(2.) Higher order modes propagate in the feed horn.

(To determine the effect of the interaction of the feed horn with the subreflector, radiation patterns were measured by displacing the subreflector a quarter wavelength from its nominal position. Small changes were observed in the radiation patterns primarily in the geometrical illumination region. The patterns also showed a cyclic dependence on the displacement of the subreflector by a half wavelength, indicating that the changes were due to reflections from the horn.)

The noise temperature due to the spillover at the main reflector has been determined by integration of the measured subreflector radiation patterns. For an illumination angle of 30.5° the noise temperature is 3.3°K. This value is in good agreement with the computed noise temperatures shown in Fig. 13.

The measured main beam portions of the antenna patterns are in agreement with the computed patterns of the main beam. The measured side lobe patterns are in reasonable agreement with the computation in the *E* plane. In the *H* plane the pattern is non-symmetric. Asymmetry in this plane can only be caused by a field with non-uniform phase in the projected antenna aperture. Possible causes are:

(1.) Deformation of the main reflector during handling.

(2.) Slight mechanical misadjustments.

(3.) Small reflection from the subreflector support and from the protruding feed horn.

VI. SUMMARY

We have built an open cassegrain antenna which has a computed efficiency exceeding 65 per cent (including spillover and scattering losses but not including ohmic loss), a calculated noise temperature less than

4°K (when the antenna is appropriately mounted and assuming earth radiation of 300°K, but not including ohmic loss), and a very acceptable near sidelobe structure.

It is perhaps more significant that analytical and experimental tools have been developed which make possible the design of an open cassegrain antenna with predictable performance. These tools, the radiation analyses and mode coupler characteristics, taken together with a conceptual understanding of the geometrical tradeoffs that can be made, permit the development of antennas to meet a variety of specific requirements in a near optimum way.

ACKNOWLEDGMENTS

Following the TELSTAR® satellite experiments, people in diverse departments of Bell Telephone Laboratories studied many antenna configurations from as many different viewpoints. The evaluation of the open cassegrain was influenced by those people, as well as by work done elsewhere through the industry; but most directly by F. T. Geyling who was active in the study program and was party to the conversation wherein the concept crystallized.

The authors gratefully acknowledge the efforts of E. R. Nagelberg and J. Shefer who designed and evaluated the mode converter for the 60-gcs antenna; K. L. Warthman who aided in the design and construction of the antenna test mount; and L. H. Hendler who assembled the antenna test equipment, and assisted in the antenna measurements. Miss G. Fischbein and H. W. Lydiksen programmed the computation of the radiation pattern from the antenna and its components.

APPENDIX A

Geometry and Location of the Main Reflector Boundary

In assembling the antenna it is necessary to precisely position the subreflector with respect to the main reflector. It has been found convenient to position it with respect to the major and minor axes of the main reflector boundary ellipse.

This ellipse is a particular ellipse of the family of ellipses generated by the intersection of the paraboloid surface with planes perpendicular to the x_p , z_p plane (Fig. 3). The equation for the ellipses in the x_0 , y plane are:

$$\cos^2 \theta_{p0} \left[x_0 - \tan \theta_{p0} \left(\frac{2f}{\cos \theta_{p0}} \right) \right]^2 + y^2 = \frac{4f\,(f - r_0 \cos \theta_{p0})}{\cos^2 \theta_{p0}} \qquad (50)$$

The curves of intersection of cones $\theta = \theta_c$ (constant) (Fig. 4) and the paraboloid surface are also ellipses. These ellipses coincide with the ellipses (50) and the following relations hold:

$$r_0 = \frac{2f \cos \theta_c}{\sqrt{1 + \cos^2 \theta_c + 2 \cos \theta_c \cos \theta_0}} \tag{51}$$

and

$$\tan \theta_{p0} = \frac{\sin \theta_0}{\cos \theta_c + \cos \theta_0}. \tag{52}$$

The major and minor dimensions of the ellipses in terms of θ_c and θ_0 are:

$$\rho_{\text{major}} = \frac{2f \sin \theta_c \sqrt{1 + \cos^2 \theta_c + 2 \cos \theta_c \cos \theta_0}}{(\cos \theta_c + \cos \theta_0)^2} \tag{53}$$

and

$$\rho_{\text{minor}} = 2f \frac{\sin \theta_c}{\cos \theta_c + \cos \theta_0}. \tag{54}$$

The radial distances from the origin, or focus, to the termini of the major and minor axes of the ellipses are:

$$r_{1,2\,\text{major}} = \frac{2f}{1 + \cos(\theta_0 \pm \theta_c)} \tag{55}$$

and

$$r_{\text{minor}} = \frac{2f\,(1 + \cos \theta_c \cos \theta_0)}{(\cos \theta_c + \cos \theta_0)^2}. \tag{56}$$

The φ coordinates of r_{minor} may be expressed:

$$\cos \varphi_{\text{minor}} = \frac{\sin \theta_c \sin \theta_0}{1 + \cos \theta_c \cos \theta_0}. \tag{57}$$

The φ coordinates of $r_{1,2\,\text{major}}$ are 0 and π, respectively.

APPENDIX B

The Symmetries of the Radiation Fields of a Horn Excited with TE_{11} and TM_{11} Modes

Consider the function,

$$F = \frac{e^{-jkR}}{R}\,(1 + 1_n \cdot 1_R). \tag{58}$$

In the two coordinate systems, referring to Fig. 8, R and $1_n \cdot 1_R$ are: In the θ_1', φ_1' coordinate system,

$$R = \sqrt{(r_1')^2 + l^2 - 2r_1'l \cos \gamma'}, \tag{59}$$

with

$$\cos \gamma' = \sin \theta'_1 \sin \theta' \cos (\varphi_1' - \varphi') + \cos \theta_1' \cos \theta' \tag{60}$$

and

$$1_n \cdot 1_R = \frac{r_1' \cos \gamma' - l}{R}. \tag{61}$$

In the θ_1, φ_1 coordinate system,

$$R = \sqrt{r_1^2 + l^2 + p^2 + 2r_1p \cos \theta_1 - 2lp \cos \theta' - 2r_1l \cos \gamma_1}, \tag{62}$$

with

$$\cos \gamma_1 = \sin \theta_1 \sin \theta' \cos (\varphi' - \varphi_1) + \cos \theta_1 \cos \theta' \tag{63}$$

and

$$1_n \cdot 1_R = \frac{p \cos \theta' - l + r_1 \cos \gamma_1}{R}. \tag{64}$$

Function F is a periodic function of the variable $(\varphi' - \varphi_1)$ and furthermore

$$F(\varphi' - \varphi_1) = F(\varphi_1 - \varphi') \tag{65}$$

in both coordinate systems. The Fourier series expansion of F is

$$F = \sum_{n=0}^{\infty} C_n(\theta',\theta_1) \cos n (\varphi' - \varphi_1). \tag{66}$$

The rectangular components of TE_{11} and TM_{11} modes in a circular waveguide for x and y polarization are:[6]

$$\begin{aligned}(\bar{E}_{a\text{TE}})_x = A_x\{1_x[J_0(k_{\text{TE}}\rho) + J_2(k_{\text{TE}}\rho) \cos 2\varphi'] \\ + 1_y J_2(k_{\text{TE}}\rho) \sin 2\varphi'\}\end{aligned} \tag{67}$$

$$\begin{aligned}(\bar{E}_{a\text{TE}})_y = A_y\{1_y[J_0(k_{\text{TE}}\rho) - J_2(k_{\text{TE}}\rho) \cos 2\varphi'] \\ + 1_x J_2(k_{\text{TE}}\rho) \sin 2\varphi'\}\end{aligned} \tag{68}$$

with

$$J_1'(k_{\text{TE}}a) = 0 \tag{69}$$

and

$$(\bar{E}_{a\mathrm{TM}})_x = B_x\{1_x[J_0(k_{\mathrm{TM}}\rho) - J_2(k_{\mathrm{TM}}\rho)\cos 2\varphi'] - 1_y J_2(k_{\mathrm{TM}}\rho)\sin 2\varphi'\} \tag{70}$$

$$(\bar{E}_{a\mathrm{TM}})_y = B_y\{1_y[J_0(k_{\mathrm{TM}}\rho) + J_2(k_{\mathrm{TM}}\rho)\cos 2\varphi'] - 1_x J_2(k_{\mathrm{TM}}\rho)\sin 2\varphi'\} \tag{71}$$

with

$$J_1(k_{\mathrm{TM}}a) = 0. \tag{72}$$

The subscripts x, y indicate x and y polarization respectively.

$J_n(_N)$ = Bessel function of order n

a = Radius of circular waveguide

For a narrow angle horn a linear relationship between δ and θ' may be assummed[7] given by

$$\rho = \alpha(\theta'/\alpha) \qquad \alpha = \text{horn angle}. \tag{73}$$

The y component of the first term of (16) is

$$(E_{py})_y = \frac{jkA_y l^2}{4\pi}\int_0^{\alpha}\int_0^{2\pi}\left[(E_{ay\mathrm{TE}})_y + \frac{B_y}{A_y}(E_{ay\mathrm{TM}})_y\right]\frac{e^{-jkR}}{R}(1 + 1_n\cdot 1_R)\sin\theta'\,d\theta'\,d\varphi' \tag{74}$$

where $(E_{ay\mathrm{TE}})_y$ and $(E_{ay\mathrm{TM}})_y$ are the y components of (68) and (71) respectively. Using (66)

$$(E_{py})_y = D_{y_0}(\theta_1) - D_{y_2}(\theta_1)\cos 2\varphi_1 \tag{75}$$

with

$$D_0(\theta_1) = \frac{jkA_y l^2}{2}\int_0^{\alpha} C_0(\theta',\theta_1)\left[J_0\left(k_{\mathrm{TE}}a\,\frac{\theta'}{\alpha}\right) + \frac{B_y}{A_0}J_0\left(k_{\mathrm{TM}}a\,\frac{\theta'}{\alpha}\right)\right]\sin\theta'\,d\theta' \tag{76}$$

$$D_2 = \frac{jkA_y l^2}{4\pi}\int_0^{\alpha} C_2(\theta',\theta_1)\left[\frac{B_y}{A_y}\,J_2\left(k_{\mathrm{TM}}a\,\frac{\theta'}{\alpha}\right) - J_2\left(k_{\mathrm{TE}}a\,\frac{\theta'}{\alpha}\right)\right]\sin\theta'\,d\theta'. \tag{77}$$

In the principal planes $\varphi_1 = 0$ and $\varphi_1 = \pi/2$

$$[E_{py}(0)]_y = D_0(\theta_1) - D_2(\theta_1) \tag{78}$$

and

$$[E_{py}(\pi/2)]_y = D_0(\theta_1) + D_2(\theta_1). \tag{79}$$

Due to the similarity of the aperture fields, by analogy

$$(E_{px})_y = D_2(\theta_1) \sin 2\varphi_1 \tag{80}$$

$$(E_{py})_x = D_2(\theta_1) \sin 2\varphi_1 \tag{81}$$

$$(E_{px})_x = D_0(\theta_1) + D_2(\theta_1) \cos 2\varphi_1 . \tag{82}$$

It is reasonable to assume that the components of radiated electric field have only components perpendicular to the radial direction. The nearly spherical wave front obtained in the coordinate system with its origin at the phase center partially justifies this assumption. In analogy to the electric field radiated from an open waveguide[6] it is assumed that

$$E_\theta = E_{px} \cos \varphi_1 + E_{py} \sin \varphi_1 \qquad (83$$

and

$$E_\varphi = E_{py} \cos \varphi_1 - E_{px} \sin \varphi_1 . \tag{84}$$

Using (75) through (84) the fields for both polarizations are (19) and (20).

Due to the φ' symmetries of the y component of the electric field it is sufficient to integrate (74) from 0 to π for $\varphi_1 = 0$ and from $-(\pi/2)$ to $(\pi/2)$ for $\varphi_1 = \pi/2$.

APPENDIX C

Construction of a Reflector Surface for the Conversion of an Equiphase Surface to a Spherical Surface

The theorem by Malus is derived for the case where the incident equiphase surface, S_i, is arbitrary and the reflected equiphase surface, S_s, is spherical. Based on the derivation, a method is presented for the construction of the reflector surface, S_r.

The surface S_i is assumed to be rotationally symmetric and consequently the surface S_r, and S_s are rotationally symmetric. The coordinates for the surfaces are shown in Fig. 27. The unit normal for S_i is 1_{r_0}.

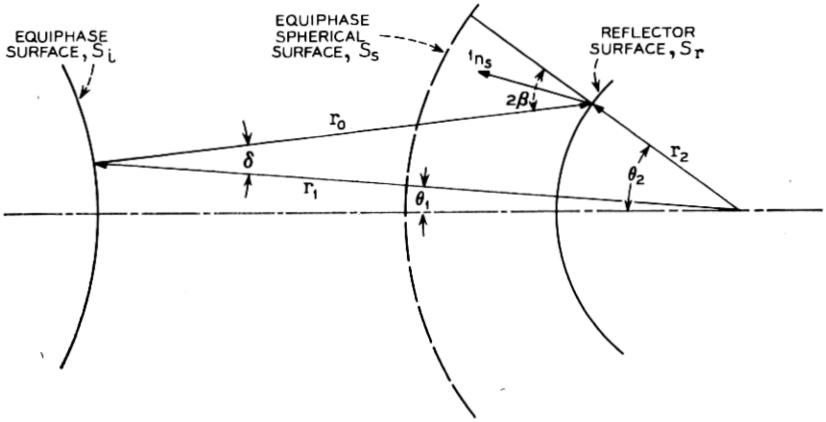

Fig. 27 — Equiphase and reflector surface coordinates.

From the geometry,

$$1_{r_1}r_1 - 1_{r_2}r_2 = -1_{r_0}r_0 . \tag{85}$$

To obtain a spherical equiphase surface it is necessary that:

$$r_0 = r_2 + a \tag{86}$$

where a is an arbitrary constant. It follows from (85) and (86) that

$$a^2 + 2r_2[r_2 \cos (\theta_2 - \theta_1) + a] - r_1^2 = 0. \tag{87}$$

The unit normal 1_{n_s} to the surface S_r is:

$$1_{n_s} = \frac{1_{r_2} - 1_{\theta_2} \dfrac{1}{r_2} \dfrac{\partial r_2}{\partial \theta_2}}{\sqrt{1 + \left(\dfrac{1}{r_2} \dfrac{\partial r_2}{\partial \theta_2}\right)^2}} \tag{88}$$

where 1_{r_2} and 1_{θ_2} are spherical vectors.

Snell's law for the surface S_r is:

$$1_{n_s} \cdot 1_{r_2} = -1_{n_s} \cdot 1_{r_0} \cdot \tag{89}$$

From (88) and (89)

$$1_{r_2} \cdot 1_{r_0} - 1_{\theta_2} \cdot 1_{r_0} \frac{1}{r_2} \frac{\partial r_2}{\partial \theta_2} = -1. \tag{90}$$

From the geometry

$$1_{r_2} \cdot 1_{r_0} = -\cos 2\beta \tag{91}$$

and

$$1_{r_2} \cdot 1_{r_2} = \sin 2\beta. \tag{92}$$

With (91) and (92), (90) reduces to

$$\frac{1}{r_2} \frac{\partial r_2}{\partial \theta_2} = \tan \beta. \tag{93}$$

Also from the geometry and (87)

$$\tan \beta = \frac{r_1 \sin (\theta_2 - \theta_1)}{r_1 \cos (\theta_2 - \theta_1) + a}. \tag{94}$$

It remains to be shown (87) and (93) are satisfied simultaneously, this is done by differentiating (87) with respect to θ_2 and considering that

$$r_2(\theta_1) = r_2[\theta_1(\theta_2)]. \tag{95}$$

Differentiating (87) results:

$$\frac{1}{r_2} \frac{\partial r_2}{\partial \theta_2} = \frac{r_1 \sin (\theta_2 - \theta_1)}{r_1 \cos (\theta_2 - \theta_1) + a} + \frac{\left\{ r_2 r_1 \sin (\theta_2 - \theta_1) + [r_2 \cos (\theta_2 - \theta_1) - r_1] \dfrac{\partial r_1}{\partial \theta_1} \right\} \dfrac{\partial \theta_1}{\partial \theta_2}}{r_2 \, [r_1 \cos (\theta_2 - \theta_1) + a]}. \tag{96}$$

Comparing (96) with (93) and (94) it follows that (87) and (93) are satisfied simultaneously provided that

$$\frac{1}{r_1} \frac{\partial r_1}{\partial \theta_1} = \frac{r_2 \sin (\theta_2 - \theta_1)}{r_1 - r_2 \cos (\theta_2 - \theta_1)}. \tag{97}$$

Since 1_{r_0} is a unit normal to the surface S_i by analogy to (93)

$$\frac{1}{r_1} \frac{\partial r_1}{\partial \theta_1} = \tan \delta = \frac{r_2 \sin (\theta_2 - \theta_1)}{r_1 - r_2 \cos (\theta_2 - \theta_1)}. \tag{98}$$

The latter equality follows the geometry. Therefore (87) and (93) are satisfied simultaneously.

The reflecting surface can be constructed as follows. Equation (86) is an equation for a hyperboloid with r_1 (the distance between the foci) and a as the defining parameters. The intersection of the hyperboloid with the line in the direction r_0, determines a point of the reflecting surface.

REFERENCES

1. Potter, P. D., A New Horn Antenna with Suppressed Side-lobes and Equal Beamwidths, Microwave J., *VI*, June 1963, pp. 71–78.
2. Nagelberg, E. R., and Shefer, J., Mode Conversion in Circular Waveguides, B.S.T.J., this issue, pp. 1321–1338.
3. Hogg, D. C., and Semplak, R. A., An Experimental Study of Near-Field Cassegrainian Antennas, B.S.T.J., *43*, Nov. 1964, p. 2677.
4. Hogg, D. C., Effective Antenna Temperatures due to Oxygen and Water Vapor
5. Hines, J. N., Li, T., and Turrin, R. H., The Electrical Characteristics of the
   in the Atmosphere, JAP, *30*, 1959, p. 1417.
   Horn-Reflector Antenna, B.S.T.J., *42*, July 1963, pp. 1187–1211.
6. Silver, S., *Microwave Antenna Theory and Design*, McGraw-Hill Book Co. Inc., New York, N. Y., 1949.
7. Li, T., and Turrin, R. H., Near Zone Field of the Conical Horn, IEEE Trans. *AP-12*, No. 6, Nov. 1964, pp. 800–802.
8. Bauer, K., The Phase Center of Aperture Rad, Arch. Elek, Ubertragung, *9*, 1955, p. 541.
9. Nagelberg, E., Fresnal Region Phase Centers of Circular Aperture Antennas, IEEE Trans. *AP-13*, May 1965, p. 479.